NMR in Biomedicine

Information based ranking of ten compartment models of diffusion weighted signal attenuation in fixed prostate tissue.

Journal:	*NMR in Biomedicine*
Manuscript ID	NBM-15-0318.R2
Wiley - Manuscript type:	Research Article
Date Submitted by the Author:	n/a
Complete List of Authors:	Liang, Sisi; Victoria University, College of Engineering and Science Panagiotaki , Eleftheria; University College London, Center for Medical Image Computing Bongers, Andre; University of New South Wales, Biological Resources Imaging Laboratory Shi, Peng; Victoria University, College of Engineering and Science Sved , Paul ; Royal Prince Alfred Hospital, Department of Urology Watson, Geoff; Royal Price Alfred Hospital, Tissue pathology and Diagnostic Oncology Bourne, Roger; University of Sydney,
Keywords:	Diffusion, Prostate, Modeling, Compartment models, Restricted diffusion, microstructure imaging

Information based ranking of ten compartment models of diffusion weighted signal attenuation in fixed prostate tissue.

Authors:

Sisi Liang — College of Engineering and Science, Victoria University, Melbourne, Australia

Eleftheria Panagiotaki — Center for Medical Image Computing, University College London, London, UK

Andre Bongers — Mark Wainright Analytical Centre, University of New South Wales, Sydney, Australia

Peng Shi — College of Engineering and Science, Victoria University, Melbourne, Australia

Paul Sved — Department of Urology, Royal Prince Alfred Hospital, School of medicine, University of Sydney, Sydney, Australia

Geoffrey Watson — Department of Tissue Pathology and Diagnostic Oncology, Royal Prince Alfred Hospital, Sydney, Australia

Roger Bourne — Discipline of Medical Radiation Sciences, Faculty of Health Sciences, University of Sydney, Sydney, Australia

Correspondence:

Roger Bourne,

Discipline of Medical Radiation Sciences, Faculty of Health Sciences,

UNIVERSITY OF SYDNEY, 75 East Street, Lidcombe, NSW, 2141, Australia

Tel: +61 2 9036 7350 Fax: +61 2 9351 9146

e: roger.bourne@sydney.edu.au

Running head:

Ten models of diffusion in prostate tissue

Key words:

Diffusion; prostate; modeling; compartment models; restricted diffusion; microstructure imaging

Word count: 3442

Abbreviations used: ADC, apparent diffusion coefficient; AIC, Akaike Information Criterion; DWI, diffusion weighted imaging; SNR, signal-to-noise ratio; DCE, dynamic contrast enhanced; mpMRI, Multiparametric MRI; DTI, diffusion tensor imaging; FA, fractional anisotropy; MD, mean diffusivity;

Title

Information based ranking of ten compartment models of diffusion weighted signal attenuation in fixed prostate tissue.

Sisi Liang, Eleftheria Panagiotaki, Andre Bongers, Peng Shi, Paul Sved, Geoffrey Watson, Roger Bourne

Abstract

This study compares the theoretical information content of single and multi-compartment models of diffusion weighted signal attenuation in prostate tissue. Diffusion weighted imaging (DWI) was performed at 9.4T with multiple diffusion times and an extended range of *b*-values in four whole formalin fixed prostates. Ten models, including different combinations of isotropic, anisotropic, and restricted components were tested. Models were ranked using Akaike's Information Criterion. In all four prostates two-component models comprising an anisotropic Gaussian component and an isotropic restricted component ranked highest in the majority of voxels. Single component models, whether isotropic (ADC) or anisotropic (DTI), consistently ranked lower than multicomponent models. Model ranking trends were independent of voxel size and maximum *b*-value in the range tested (1.6-16 mm^3 and 3000-10,000 s/mm^2). This study characterizes the two major water components previously identified by biexponential models and shows that models incorporating both anisotropic and restricted components provide more information-rich descriptions of DWI signals in prostate tissue than single or multicomponent anisotropic models and models that do not account for restricted diffusion.

Key words: diffusion; prostate; modeling; compartment models; restricted diffusion; microstructure imaging

Introduction

At present the optimum choice of therapy for prostate cancer, and even whether therapy is warranted, remains unclear and controversial. While it is well established that the best indicator of cancer aggressiveness is the grade and volume of cancer, at present this can only be measured reliably after removal of the prostate (1-3). Multiparametric MRI (mpMRI) combining T_2-weighted, dynamic contrast enhanced (DCE), and diffusion weighted imaging (DWI) is increasingly being used to assist targeted biopsy, risk stratification, and treatment selection for prostate cancer (4-6). The sensitivity and specificity of the three methods combined is usually higher than for any one method alone, however, DWI shows stronger correlations with both cancer grade and volume than T_2 and DCE (7-9).

The superior cancer detection performance of DWI is remarkable because the standard method – calculation of an apparent diffusion coefficient (ADC) using a monoexponential signal model – is highly simplistic and assumes a Gaussian spin displacement behavior that is well known to be invalid in biological tissue (10). The success of simple ADC-based prostate cancer detection can be attributed to the direct relationship between DWI signal attenuation and the tissue microstructural features that define the presence and grade of cancer (11), and suggests that more sophisticated DWI acquisitions and signal analysis methods are likely to significantly improve the performance of mpMRI. Phenomenological approaches have demonstrated that DWI measurements over an extended range of *b*-values are inherently more information-rich than an ADC model would suggest (12,13), and may provide more accurate detection of prostate cancer in clinical prostate imaging (14-16). However, in general, phenomenological models of measured signals do not provide parameter values that can be directly related to tissue structure properties.

Ideally, models for cancer assessment would be based on tissue microstructure. To this end, a three-component 'VERDICT' model based on vascular, extravascular/extracellular, and intracellular compartments has recently been shown to provide more reliable discrimination of cancer and normal tissue than monoexponential and biexponential signal models, and to return model parameters consistent with histological features such as average cell diameter (17). A significant innovation of VERDICT is the inclusion of a restricted diffusion component (the putative intracellular compartment), the fitting of which requires DWI signal acquisition at multiple diffusion times.

Previous prostate studies utilizing the VERDICT framework in a clinical setting (18,19) used only isotropic compartment models. A recent study of diffusion anisotropy in prostate tissue using a conventional diffusion tensor imaging (DTI) model reported wide variations in mean voxel fractional anisotropy (FA) between prostates and a strong voxel size dependency with FA decreasing as voxel size increases (20). Diffusion microimaging of fixed prostate tissue demonstrates high anisotropy in the fibromuscular stroma and low FA in the glandular epithelium and lumen spaces (21). A typical clinical DWI sized voxel (volume 4-16 mm^3) is likely to contain a mixture of isotropic and anisotropic compartments. A single component DTI model will have limited ability to detect the actual anisotropy of the stromal component if the partial volumes of epithelium and lumen space are significant. Multi-compartment models that include at least one anisotropic component would be expected to provide a more precise description of such sub-voxel heterogeneity than DTI and isotropic models.

In the study presented here we investigate the relative information content of compartment models that include anisotropic components and test the importance of inclusion of a restricted diffusion compartment. To obtain 'ground truth' data to inform the further development of clinical imaging methods we performed these studies in the absence of perfusion effects using radical prostatectomy specimens and high signal-to-noise ratio (SNR) measurements which enable model fitting with fewer parameter constraints than in previous applications of the VERDICT model.

Methods

Tissue Handling and Histopathology

The study was conducted with institutional ethics approval and written informed consent from all patients. Four whole prostates were imaged: Prostate 1, age 59y, 47g, Gleason 4+4; Prostate 2, age 57y, 38g, Gleason 3+3; Prostate 3, 56y, 47g, Gleason 3+4; Prostate 4, normal prostate, 35g, from cystoprostatectomy for bladder cancer. The intact organ was sent to the pathology department immediately upon surgical resection and without immersion in a fixative solution. The organ was weighed and inked and the seminal vesicles and any surgical clips were removed prior to transport and imaging of the unfixed tissue (for investigations not reported here). The total time between resection and immersion in formalin was 6-8 hr. A specialist urological pathologist confirmed no significant tissue degradation due to delayed fixation of the specimens. Following immersion in 10% neutral buffered formalin for 24 hr, the fixed prostate was soaked in saline for 24 hr before imaging for 24-48 hr and then returned to the hospital pathology department for routine processing. Prostates were sectioned at 4-mm intervals in planes orthogonal to a tube inserted through the urethra and parallel to the imaging slices (see below). All the measurements reported here were performed on the fixed specimens.

MR Imaging

Prostates 1 and 2 were scanned with nominal *b*-value range 50-3000 s/mm^2 and voxel size 2×2×4 mm^3 to emulate feasible clinical voxel sizes and *b*-values. Prostates 3 and 4 were imaged at high spatial resolution (voxel size 1×0.78×2 mm^3 and 1.4×1.4×2 mm^3 respectively) over an extended *b*-value range of 50-10354 s/mm^2. The use of a range of acquisition parameters tests the generality of the model selection and intentionally includes protocols feasible in clinical scanners together with methods only possible with high gradients and ex vivo samples. The range of voxel sizes used tests for any effect of variation in subvoxel tissue heterogeneity.

Each organ was imaged suspended on a 5-mm saline-filled NMR tube inserted through the urethra and mounted in brackets in a plastic casing that maintained the tube axis parallel to and approximately 5 mm above the magnet Z-axis (22). Imaging was performed at room temperature (22°C) on a 9.4T Bruker (Bruker, Karlsruhe, Germany) BioSpec Avance III 94/20 magnetic resonance microimaging system equipped with a 72-mm internal diameter quadrature radiofrequency coil and BGA-12S HP gradients with maximum strength 660 mT/m and slew rate 4570 T/m/s. Imaging was performed transaxial to the urethra with the imaging planes oriented orthogonal to the 5-mm NMR tube. A paint landmark was used to identify the central imaging plane for later sectioning of the organ (see above).

For all prostates, diffusion encoding used a pulse-gradient spin-echo method with three orthogonal diffusion encoding gradient directions. All diffusion weighted measurements were preceded by the acquisition of two reference '*b* = 0' images. Intrinsic SNR was calculated from a large intraprostatic region of interest in a pair of reference images (23). Additional DTI acquisitions were performed using a 6-direction scheme. DWI and DTI acquisition parameters are detailed in Table 1.

Model Description

Models with one to three compartments were tested with components described according to the taxonomy used for brain tissue DWI in (24). The individual components (Table 2) that were combined to create the multi-compartment models included: 1) a conventional single-component DTI model, which provides two commonly used summary parameters FA and mean diffusivity (MD) (25); 2) a Zeppelin, which is a cylindrically symmetric tensor that also provides FA and MD; 3) a Ball which is an isotropic tensor; and 4) as in (17), a Sphere compartment describing restricted diffusion within a non-zero radius spherical pore. Each model compartment was fitted individually and in a variety of combinations to test and evaluate in total ten models (Table 3).

Model Fitting

A wide range of imaging parameters was used to ensure stable fitting (17). DWI measurements included 3-direction data with multiple *b*-values and multiple Δ and δ values, combined with single *b*-value and single δ/Δ-value 6-direction data to enable fitting of anisotropic components. The acquisition of data at multiple diffusion times enables estimation of a restriction radius based on the diffusion time dependence of the apparent diffusion coefficient. Each model was fitted to the combined 3- and 6-direction data using the Levenberg-Marquardt minimization algorithm in the open source Camino toolkit (26). To minimize any possible T_2 effects data were normalized to the 'b=0' signal prior to fitting (17). Model fitting was based on minimization of an objective function that uses an offset-Gaussian noise model to account for the inherent Rician distributed noise in the magnitude MRI data (17). Model parameters were constrained within meaningful biophysical limits. Radius R of the isotropic restricted 'sphere' component was constrained to the range 0.1-20 μm according to typical cell diameter. All component signal fractions were constrained to a range of 0-1 and sum to 1. Diffusivities were constrained so that $0 \le D \le 2.1$ μm^2/ms according to the 22°C sample temperature (27).

Model Ranking

Models were ranked using the Akaike Information Criterion (AIC) which compares models in terms of theoretical information content (28). AIC provides an estimate of the relative distance of competing models from the (usually unknowable) system truth and avoids the use of arbitrary cutoffs required for hypothesis testing. In prostate tissue AIC-based model ranking has previously been shown to be consistent with a leave-one-out test of model prediction accuracy (12,13). Differences between model ranking AIC scores were assessed via a Mann-Whitney U-Test performed in Matlab.

Results

Figure 1 summarizes variation in model rankings based on AIC and shows the anatomical distribution of the highest ranked models in a mid-organ transverse slice of each prostate. Figure 2 shows the rank variations of the individual models, and Fig. 3 provides box and whiskers plots of the variation in AIC scores within and between models for each prostate. Log(AIC) data is presented in Fig. 3 as this produced a normal distribution of the skewed raw AIC scores.

In all four prostates either the Zeppelin-sphere or Tensor-sphere model was ranked highest in the large majority of voxels. There was no distinct variation of ranking according to prostate zonal anatomy (not assessed quantitatively). The differences between eigenvalues of the Tensor and Zeppelin components of these models were minor (data not shown). The only other model that included a restricted component, the Ball-sphere, ranked close to Zeppelin-sphere and Tensor-sphere. The single component Ball (ADC) and DTI models ranked low in all prostates. In general, multi-component models that included one or two anisotropic components ranked higher than models that did not account for anisotropy, and models that included a restricted diffusion compartment ranked higher than those that did not. Model ranking trends were largely independent of voxel size, maximum *b*-value, maximum diffusion time, and whether or not two different diffusion encoding pulse lengths (δ) were used (Table 1).

Results of a Mann-Whitney U-test for significant differences between AIC scores are presented in the supplementary material available online. The statistical analysis shows that the AIC ranking suggests three primary groups: 1) Zeppelin-sphere, (Tensor-sphere); 2) Ball-zeppelin, (Ball-sphere), Bi-ball-zeppelin, Bi-zeppelin, Ball-tensor; 3) Ball, (Bi-ball), DTI. The brackets indicate models that may appear in other group in some prostates. The Group 1 models have significantly lower AIC scores than Group 2 and 3 models, consistent with the qualitative data presented in Figs 1 and 2.

These results indicate that two-component Zeppelin-sphere and Tensor-sphere models that account for both anisotropy and diffusion restriction provide more information-rich descriptions of multi-Δ, multi-*b* DWI measurement data than simpler isotropic, DTI, and unrestricted models.

Figure 4 provides a visual illustration the fit of the ten models to summed data from a homogeneously anisotropic four-voxel region of interest in normal transition zone tissue. Although the DTI-estimated anisotropy of the four voxels was low (range 0.17-0.20) the highest six AIC-ranked models all include at least one anisotropic component and provide better fits to the measurement data than the isotropic models and the single component DTI model. Nevertheless, it is also evident that not even the most highly parameterized models provide an exact description of the measurement data, indicating signal modulation effects that these models do not capture.

Parametric maps derived from the Zeppelin-sphere model are presented in Figure 5 together with mapped pathology from approximately the same slice location. The Ball-*D* parameter map (ADC) is included for reference. Very similar parameter maps were obtained for the Tensor-sphere model (Supporting Figure S1).

Parameter histogram images for the Zeppelin-sphere model are shown in Figure 6. The histograms are presented as *D* or *R* versus component signal fraction. When the component signal fraction is low the bias and variance for that component's parameters would be expected to be higher than when the signal fraction (and hence the component SNR) is high. In the majority of voxels the diffusivity parameter values are biophysically plausible (less than the diffusion coefficient for pure water at 22^{o}C (29)). The sphere radius parameter value range (Fig. 6) is also consistent with typical cell diameters. Simple histograms of *D* and *R* are provided in Supplementary Figure S2.

Discussion

This study extends previous comparisons of phenomenological isotropic single and two component models of DWI signals measured ex vivo in prostate tissue. Bourne et al. (12) found that for measurements including *b*-values above 2000 s/mm^2 (at δ/Δ = 5/20 ms) a biexponential model had a higher information content than monoexponential (ADC), stretched exponential, and kurtosis models. Hall et al. (13) examined the value of the stretched exponential as a modifier of the 'slow' and 'fast' components of the biexponential model, demonstrating that at all diffusion times tested (8, 18, and 38 ms) the 'slow' water pool exhibits distinctly non-Gaussian displacement dynamics. The 'fast' water pool tended towards Gaussian behavior at the longer diffusion times. Whilst those studies clearly demonstrate the presence of two distinct spin pools, a limitation was the lack of modeling of diffusion anisotropy and restricted diffusion. The 'slow' non-Gaussian water pool described by Hall et al. most probably corresponds to the restricted sphere component of our models, and the 'fast' component to our anisotropic component.

The study presented here suggests that both anisotropic and restricted components are required to accurately describe DWI signals measured over an extended range of *b*-values and multiple diffusion times. The consistentently high ranking of the anisotropic+restricted two component models over a range of voxel sizes strongly suggests that the spin pools represented by the two components exist on a microscopic scale and that any tissue heterogeneity on a mesoscopic scale (for example variations in gland density) does not produce significant partial volume effects for the voxel sizes measured in this study.

Our results are consistent with Bourne et al. (12) and Hall et al. (13) in demonstrating the relatively poor performance of single component (ADC/Ball and DTI) models and the isotropic biexponential (Bi-ball) model. It is noteworthy that to date ADC and DTI models have been the most commonly used analysis of in vivo prostate DWI measurements, and that ADC is a cornerstone of the mpMRI-based prostate cancer assessment protocol (4-6). The low AIC ranking of ADC and DTI models in this study suggests that the performance of DWI in prostate cancer assessment might be improved by implementation of more sophisticated DWI protocols such as the three-component structure-based 'VERDICT' model (18).

Comparison with VERDICT model

VERDICT (18) has been utilized to quantify and map histological features of prostate tissue based on in vivo multi-Δ, multi-b DWI measurements. The results suggest VERDICT can discriminate benign and cancerous tissue better than ADC (Ball), kurtosis, and biexponential (Bi-ball, or intravascular incoherent motion (30)) models. The three components of the VERDICT model are based on vascular, extravascular/extracellular, and intracellular compartments. The prostate-specific form of the generic VERDICT model is designed to account for: 1) water trapped in cells (modeled as a sphere component); 2) interstitial water (modeled as an isotropic diffusion tensor); and 3) water in the vasculature (modeled as restricted water in cylinders with uniformly distributed orientations and zero diameter) (18,19). Our study of unperfused prostate tissue ex vivo provides further information about the 'true diffusion' (non-perfusion) components of the VERDICT model, and in particular demonstrates the presence of a significant anisotropic diffusion component.

An important difference between our model fitting strategy and VERDICT is the number of fitted parameters. The large number of b-values and high SNR of our measurements enabled the reliable (low parameter variance) fitting of more highly parameterized models with fewer constraints on parameter values. When applying the VERDICT model to in vivo prostate data all component diffusivities (including the pseudodiffusion coefficient of the vascular component) were fixed to values previously found to minimize an objective function ('fitting error') over all voxels (18), all three components were isotropic, and only three independent parameters were fitted (intravascular volume fraction, extracellular extravascular volume fraction, and sphere radius). These constraints were necessary to avoid overfitting of the relatively noisy in vivo data.

In contrast to in vivo prostate VERDICT model fitting we permitted all diffusion coefficients to float within biophysical limits and allowed for diffusion anisotropy with the Tensor and Zeppelin components. In the large majority of voxels the fitting returned parameter values inside the defined limits, a strong indication that the models are biophysically plausible. The superior AIC performance of the minimally constrained multi-component anisotropic and restricted diffusion models over the isotropic, unrestricted, and single component anisotropic models indicates that the parameter values of these less constrained models contain information about the tissue microstructure.

When applying the VERDICT model to in vivo prostate DWI data, Panagiotaki et al. constrained the 'true' diffusivity parameters (intracellular water and extracellular extravascular water) to a fixed value of 2 μm^2/ms (18), which corresponds to ~1.4 μm^2/ms at 22^{o}C (27). The value of 1.4 μm^2/ms is consistent with the main peaks in the Zeppelin diffusivity histograms of our data (Fig. 6).

The high ranking of the Tensor-sphere, Zeppelin-sphere, and Ball-sphere models in the majority of voxels in all four prostates, even in the absence of fixed diffusivity parameter values, indicates the importance of accounting for restricted diffusion in any modeling of prostate tissue and supports the inclusion of a restricted component in VERDICT.

Cancer detection

Our study demonstrates that for DWI measurements over an extended *b*-value range and including multiple diffusion times the anisotropic/restricted diffusion models have higher theoretical information content than conventional ADC and DTI models. Nevertheless, it should be noted that it is possible that this information does not have any extra value for identification of pathology. The small number of prostates included in this study precludes a quantitative assessment of the value of the tested models for cancer detection. The information-based ranking of models we applied balances the tradeoff between parameter bias and variance, and *predicts* the relative ability of models to explain measurement data (28). While many published studies compare the cancer detection performance of different DWI signal models in terms of correlation of individual model parameters with tissue pathology this approach neglects the possibility that the pathology-specific (diagnostic) information is distributed between two or more model parameters (12,31). Whatever signal model is employed, it is also possible that the imaging method (eg. diffusion times, *b*-values, gradient orientations) does not provide appropriate data for pathology discrimination. Information theory defines the most likely useful model(s), the pathology detection performance of which should then be assessed by correlation of single and combined parameters with accurately matched pathology data from a large number of samples.

Limitations

This study has several limitations. Imaging of the tissue ex vivo enables acquisition of high spatial resolution high SNR data free from movement and other artifacts, and free from perfusion effects, but the absence of perfusion may result in a decreased volume of extravascular extracellular water which would be expected to have some effect on the signal fractions for each compartment.

Formalin fixation stabilizes the tissue against degradation by cross-linking of protein but consequently leads to a decrease in measured tissue diffusivities (22,32). Previous studies suggest this is unlikely to affect model ranking (12,33).

To maximize SNR we used the minimum available echo time for each diffusion time and normalized the measurements to the maximum (‘$b = 0$’) signal to minimize any effects of T_2 heterogeneity. While there is some evidence for the existence of sub-voxel T_2 heterogeneity in prostate tissue (34,35), it is not clear that the apparently distinct T_2 water pools correspond to the two main water pools identified in multi-*b* DWI studies. This is an important topic for future investigation.

The models we tested assumed no exchange of water between compartments. To our knowledge exchange has yet to be investigated in prostate tissue. Having defined relatively simple models, such as Zeppelin-sphere, that appear to provide robust descriptions of rich data such as we acquired in these experiments, a logical next step would be to assess the value of accounting for exchange between the two compartments.

The differences between our 9.4T ex vivo measurement conditions and in vivo imaging include temperature, perfusion, tissue fixation, *b*-value range, diffusion time range, available diffusion encoding gradient strength, echo time, and SNR. Although our results cannot be directly related to in vivo prostate imaging they define some of the tissue structure properties that can be detected by DWI and emphasize a significant potential of DWI that goes currently unrealized in simple ADC and DTI techniques. The results provide basic science evidence to guide the further development of promising compartment models such as VERDICT.

CONCLUSIONS

When DWI is performed in prostate tissue over an extended range of *b*-values with multiple diffusion times compartment models incorporating both anisotropic and restricted components provide more information-rich descriptions of signals than single component models or multicomponent anisotropic models and models that do not account for restricted diffusion. These results highlight the limitations of the basic ADC and DTI models and demonstrate that appropriate DWI measurements can probe multiple tissue structure features.

Acknowledgements. This work was supported by Australian NHMRC grant 1026467 and European/UK grants EPSRC H046410, G00748 and CRUK/EPSRC C1519/ A16463

References

1. Guzzo TJ, Vira M, Hwang WT, D'Amico A, Tomaszewski J, Whittington R, Wein AJ, VanArsdalen K, Malkowicz SB. Impact of multiple biopsy cores on predicting final tumor volume in prostate cancer detected by a single microscopic focus of cancer on biopsy. Urology. 2005; 66(2): 361-365.
2. Nelson BA, Shappell SB, Chang SS, Wells N, Farnham SB, Smith JA, Jr., Cookson MS. Tumour volume is an independent predictor of prostate-specific antigen recurrence in patients undergoing radical prostatectomy for clinically localized prostate cancer. BJU International. 2006; 97(6): 1169-1172.
3. Hong MK, Namdarian B, Corcoran NM, Pedersen J, Murphy DG, Peters JS, Harewood L, Sapre N, Rzetelski-West K, Costello AJ. Prostate tumour volume is an independent predictor of early biochemical recurrence in a high risk radical prostatectomy subgroup. Pathology. 2011; 43(2): 138-142.
4. Kirkham AP, Haslam P, Keanie JY, McCafferty I, Padhani AR, Punwani S, Richenberg J, Rottenberg G, Sohaib A, Thompson P, Turnbull LW, Kurban L, Sahdev A, Clements R, Carey BM, Allen C. Prostate MRI: who, when, and how? Report from a UK consensus meeting. Clin. Radiol. 2013; 68(10): 1016-1023.
5. Dickinson L, Ahmed HU, Allen C, Barentsz JO, Carey B, Futterer JJ, Heijmink SW, Hoskin PJ, Kirkham A, Padhani AR. Magnetic resonance imaging for the detection, localisation, and characterisation of prostate cancer: recommendations from a European consensus meeting. Eur. Urol. 2011; 59(4): 477-494.
6. Padhani AR, Collins D, Hammoud DA, Rustin GJS, Taouli B, Choyke PL, Liu G, Koh DM, Chenevert TL, Thoeny HC, Takahara T, Dzik-Jurasz A, Ross BD, Van Cauteren M. Diffusion-weighted magnetic resonance imaging as a cancer biomarker: consensus and recommendations. Neoplasia. 2009; 11(2): 102-125.
7. Isebaert S, Van den Bergh L, Haustermans K, Joniau S, Lerut E, De Wever L, De Keyzer F, Budiharto T, Slagmolen P, Van Poppel H. Multiparametric MRI for prostate cancer localization in correlation to whole‐mount histopathology. J. Magn. Reson. Imaging. 2013; 37(6): 1392-1401.
8. Selnæs KM, Heerschap A, Jensen LR, Tessem M-B, Jarosch-Von Schweder G, Goa PE, Viset T, Angelsen A, Gribbestad IS. Peripheral zone prostate cancer localization by multiparametric magnetic resonance at 3 T: unbiased cancer identification by matching to histopathology. Invest. Radiol. 2012; 47(11): 624-633.
9. Turkbey B, Shah VP, Pang Y, Bernardo M, Xu S, Kruecker J, Locklin J, Baccala Jr AA, Rastinehad AR, Merino MJ. Is apparent diffusion coefficient associated with clinical risk scores for prostate cancers that are visible on 3-T MR images? Radiology. 2011; 258(2): 488-495.
10. LeBihan D. Molecular diffusion, tissue microdynamics and microstructure. NMR Biomed. 1995; 8(7): 375-386.
11. Epstein JI, Allsbrook Jr WC, Amin MB, Egevad LL, Committee IG. The 2005 International Society of Urological Pathology (ISUP) consensus conference on Gleason grading of prostatic carcinoma. Am. J. Surg. Pathol. 2005; 29(9): 1228-1242.
12. Bourne RM, Panagiotaki E, Bongers A, Sved P, Watson G, Alexander DC. Information theoretic ranking of four models of diffusion attenuation in fresh and fixed prostate tissue ex vivo. Magn. Reson. Med. 2014; 72(5): 1418-1426.

13. Hall MG, Bongers A, Sved P, Watson G, Bourne RM. Assessment of non‐Gaussian diffusion with singly and doubly stretched biexponential models of diffusion‐weighted MRI (DWI) signal attenuation in prostate tissue. NMR Biomed. 2015; 28(4): 486-495.
14. Shinmoto H, Oshio K, Tamura C, Soga S, Okamura T, Yamada K, Kaji T, Mulkern RV. Diffusion-weighted imaging of prostate cancer using a statistical model based on the gamma distribution. J. Magn. Reson. Imaging. 2015; 42(1): 56-62.
15. Shinmoto H, Oshio K, Tanimoto A, Higuchi N, Okuda S, Kuribayashi S, Mulkern RV. Biexponential apparent diffusion coefficients in prostate cancer. Magn. Reson. Imaging. 2009; 27(3): 355-359.
16. Rosenkrantz AB, Sigmund EE, Johnson G, Babb JS, Mussi TC, Melamed J, Taneja SS, Lee VS, Jensen JH. Prostate cancer: feasibility and preliminary experience of a diffusional kurtosis model for detection and assessment of aggressiveness of peripheral zone cancer. Radiology. 2012; 264(1): 126-135.
17. Panagiotaki E, Walker-Samuel S, Siow B, Johnson SP, Rajkumar V, Pedley RB, Lythgoe MF, Alexander DC. Noninvasive quantification of solid tumor microstructure using VERDICT MRI. Cancer Res. 2014; 74(7): 1902-1912.
18. Panagiotaki E, Chan R, Dikaios H, Ahmed HU, O'Callaghan J, Freeman A, Atkinson D, Punwani S, Hawkes D, Alexander D. Microstructural Characterization of Normal and Malignant Human Prostate Tissue With Vascular, Extracellular, and Restricted Diffusion for Cytometry in Tumours Magnetic Resonance Imaging. Invest. Radiol. 2015; 50(4):218-227.
19. Panagiotaki E, Andrada I, Johnston E, Chan R, Stevens N, Atkinson D, Punwani S, Hawkes D, Alexander D. Optimised VERDICT MRI Protocol for Prostate Cancer Characterisation. *Proceedings of the 23rd Annual Meeting ISMRM*, Toronto, Canada, 2015; 2872.
20. Bourne RM, Bongers A, Chatterjee A, Sved P, Watson G. Diffusion anisotropy in fresh and fixed prostate tissue ex vivo. Magn. Reson. Med. 2015: Early view. doi: 10.1002/mrm.25908.
21. Bourne RM, Kurniawan N, Cowin G, Sved P, Watson G. Microscopic diffusion anisotropy in formalin fixed prostate tissue: Preliminary findings. Magn. Reson. Med. 2012; 68(6): 1943-1948.
22. Bourne R, Bongers A, Charles N, Power C, Sved P, Watson G. Effect of formalin fixation on biexponential modeling of diffusion decay in prostate tissue. Magn. Reson. Med. 2013; 70(4): 1160-1166.
23. Dietrich O, Raya JG, Reeder SB, Reiser MF, Schoenberg SO. Measurement of signal‐to‐noise ratios in MR images: Influence of multichannel coils, parallel imaging, and reconstruction filters. J. Magn. Reson. Imaging. 2007; 26(2): 375-385.
24. Panagiotaki E, Schneider T, Siow B, Hall MG, Lythgoe MF, Alexander DC. Compartment models of the diffusion MR signal in brain white matter: a taxonomy and comparison. Neuroimage. 2012; 59(3): 2241-2254.
25. Basser PJ. Inferring microstructural features and the physiological state of tissues from diffusion-weighted images. NMR Biomed. 1995; 8(7): 333-344.
26. Cook P, Bai Y, Nedjati-Gilani S, Seunarine K, Hall M, Parker G, Alexander D. Camino: open-source diffusion-MRI reconstruction and processing. *Proceedings of the 14th Annual Meeting ISMRM*, Seattle, WA, USA, 2006; 2759.
27. Weingärtner H. Self diffusion in liquid water. A reassessment. Z. Phys. Chem. 1982; 132(2): 129-149.

28. Burnham KP, Anderson DR. *Model selection and multimodel inference: a practical information-theoretic approac*h. Springer Science & Business Media; 2002.
29. Holz M, Heil SR, Sacco A. Temperature-dependent self-diffusion coefficients of water and six selected molecular liquids for calibration in accurate 1H NMR PFG measurements. Phys. Chem. Chem. Phys. 2000; 2(20): 4740-4742.
30. Le Bihan D, Breton E, Lallemand D, Aubin ML, Vignaud J, Lavaljeantet M. Separation of diffusion and perfusion in intravoxel incoherent motion MR imaging. Radiology. 1988; 168(2): 497-505.
31. Jambor I, Merisaari H, Taimen P, Boström P, Minn H, Pesola M, Aronen HJ. Evaluation of different mathematical models for diffusion-weighted imaging of normal prostate and prostate cancer using high b-values: A repeatability study. Magn. Reson. Med. 2015; 73(5): 1988-1998.
32. Xu JQ, Humphrey PA, Kibel AS, Snyder AZ, Narra VR, Ackerman JJH, Song SK. Magnetic Resonance Diffusion Characteristics of Histologically Defined Prostate Cancer in Humans. Magn. Reson. Med. 2009; 61(4): 842-850.
33. Richardson S, Siow B, Panagiotaki E, Schneider T, Lythgoe MF, Alexander DC. Viable and fixed white matter: Diffusion magnetic resonance comparisons and contrasts at physiological temperature. Magn. Reson. Med. 2014; 72(4): 1151-1161.
34. Storas T, Bongers A, Power C, Bourne R. Effect of Formalin Fixation on Biexponential Modeling of T1 and T2 Decay in Prostate Tissue. *Proceedings of the 21st Annual Meeting ISMRM*, Salt Lake City, Utah, USA, 2013; 1792.
35. Storas TH, Gjesdal KI, Gadmar OB, Geitung JT, Klow NE. Prostate Magnetic Resonance Imaging: Multiexponential T2 Decay in Prostate Tissue. J. Magn. Reson. Imaging. 2008; 28(5): 1166-1172.

Tables

Table 1. DWI acquisition parameters

Prostate	1	2		3			4	
FOV (mm^2)	64×50	64×50		50×50			45×45	
Matrix size	32×25	32×25		50×50			45×45	
Voxel size (mm^3)	2×2×4	2×2×4		1×0.78×2			1.4×1.4×2	
SNR	225	232		291			240	
TR (ms)	2000	2000		2000			2000	
δ (ms)	5	5	10	5	5	10	5	10
Δ (ms)	10, 20, 40, 60, 80	10, 20, 40, 60, 80	40, 60, 80	10	20, 40	20, 40	20, 40, 80	20, 40, 80
TE (ms) (=Δ + 8 ms)	18, 28, 48, 68, 88	18, 28, 48, 68, 88	93, 93, 93	18	28, 48	33, 53	28, 48, 88	28, 48, 88
b-value (s/mm^2) 6-directions	1500	1500		1500			1599	
b-value [a] (s/mm^2) 3-directions	50, 147, 275, 430, 607, 806, 1024, 1259, 1512, 1780, 2064, 2362, 2674, 3000	50, 147, 275, 430, 607, 806, 1024, 1259, 1512, 1780, 2064, 2362, 2674, 3000	50, 147, 275, 430, 607, 806, 1024, 1259, 1512, 1780, 2064, 2362, 2674, 3000	50, 178, 373, 632, 951, 1328, 1761, 2249, 2790, 3384, 4029, 4724, 5470, 5960	50, 178, 373, 632, 951, 1328, 1761, 2249, 2790, 3384, 4029, 4724, 5470, 6265, 7108, 8000	216, 511, 940, 1507, 2217, 3073, 4077, 5231, 6538	105, 279, 589, 1044, 1646, 2403, 3318, 4394, 5631, 7036, 8610, 10354	105, 279, 589, 1044, 1646, 2403, 3318, 4394, 5631, 7036, 8610, 10354

a) Nominal *b*-value. Effective *b*-values were used for model fitting.

Table 2. Model components

Name	Description	Parameters [a]
Ball (ADC)	Isotropic Gaussian diffusion	S_0 D
Zeppelin	Anisotropic cylindrically symmetric Gaussian diffusion	S_0 $D_{\|}$ $D_{\perp}$ θ ϕ
Tensor	Anisotropic Gaussian diffusion	S_0 $D_{\|}$ $D_{\perp 1}$ $D_{\perp 2}$ θ ϕ α
Sphere	Restricted diffusion inside an impermeable spherical confinement of non-zero radius *R*	S_0 D R

a) S_0, the signal at b = 0, is omitted if signal is normalized. D is a diffusivity and θ, ϕ, α are tensor angles. Detailed parameter descriptions are provided in (24)

Table 3. Fitted models

Name	Components from Table 2	Fitted parameters [a]	No. parameters
Ball (ADC)	Ball	D	1
Bi-ball	Ball + Ball	$f_1 \quad D_1 \quad D_2$	3
Ball-sphere	Ball + Sphere	$f_1 \quad D_1 \quad R \quad D_2$	4
DTI	Tensor	$D_{\parallel} \quad D_{\perp 1} \quad D_{\perp 2} \quad \theta \quad \phi \quad \alpha$	6
Ball-zeppelin	Ball + Zeppelin	$f_1 \quad D_{\parallel} \quad D_{\perp} \quad \theta \quad \phi \quad D$	6
Zeppelin-sphere	Zeppelin + Sphere	$f_1 \quad D \quad R \quad D_{\parallel} \quad D_{\perp} \quad \theta \quad \phi$	7
Ball-tensor	Ball + Tensor	$f_1 \quad D_{\parallel} \quad D_{\perp 1} \quad D_{\perp 2} \quad \theta \quad \phi \quad \alpha \quad D$	8
Bi-ball-zeppelin	Ball + Ball + Zeppelin	$f_1 \quad f_2 \quad D_1 \quad D_2 \quad D_{\parallel} \quad D_{\perp} \quad \theta \quad \phi$	8
Bi-zeppelin	Zeppelin + Zeppelin	$f_1 \quad D_{\parallel 1} \quad D_{\perp 1} \quad \theta_1 \quad \phi_1 \quad D_{\parallel 2} \quad D_{\perp 2} \quad \theta_2 \quad \phi_2$	9
Tensor-sphere	Tensor + Sphere	$f_1 \quad D_{\perp 1} \quad D_{\perp 2} \quad \theta \quad \phi \quad \alpha \quad D \quad R$	9

a) Signal normalized before fitting ($S_0 = 1$). Sum of signal fractions $f_1 + f_2 + f_n = 1$. Parameter descriptions are detailed in (24).

Figure Captions

Figure 1. Variation of model rankings in four prostates.

A) Anatomical distribution of the highest ranked model in a mid-organ slice from each prostate. (See Fig. 2 for pathology maps of these slices). Voxel color indicates model according to the Model key. The Zeppelin-sphere (yellow) or Tensor-sphere (orange) models ranked highest in most voxels in all prostates.

B) Variation of model rank positions. The grey scale indicates the number of times each model ranked at each position (eg. the Ball model ranked 10th in nearly all voxels). The model order (vertically) is based on trends assessed subjectively. See Fig. 3 for statistical summary of AIC ranks.

Data from 558 voxels from slices 5&6 in Prostate 1, 504 voxels from slices 5&6 in Prostate 2, 1278 voxels from slices 7-9 in Prostate 3, and 2041 voxels from slices 3-6 in Prostate 4.

Model Key: The three models containing a restricted component are shown with a heavy black border. Models with an anisotropic component are shown as ellipses. Vertical lines indicate number of components. Models including a restricted component are marked with an asterisk.

Figure 2. Variation in rankings of individual models in four prostates.
Slice positions as for Figs 1 and 5. Voxel color indicates model rank and models are grouped according to predominant rank.

Figure 3. Box and whiskers plots of log(AIC).

Models including a restricted component are marked with a black asterisk. For each blue box, the central red mark is the median and the top and bottom edges of the box are the 25th and 75th percentiles. The whiskers extend to the most extreme data points that are not considered outliers. Outliers are plotted individually in red.
Distributions were normal after the log transformation. Data from 558 voxels from slices 5&6 in Prostate 1, 504 voxels from slices 5&6 in Prostate 2, 1278 voxels from slices 7-9 in Prostate 3, and 2041 voxels from slices 3-6 in Prostate 4. Results for Mann-Whitney U-test are presented in Supplementary Material available online.

Figure 4. Representative model fit data.
Measurement data (symbols) and model fit (lines). Normalized signal S is plotted for all values of Δ and δ as a function of gradient strength $|G|$ for x, y, z directions. Indicated model rank is specific to this data set. Measurement data (SNR ~600) is the average from four adjacent $1 \times 0.78 \times 2$ mm^3 voxels in the transition zone of Prostate 3 with similar primary eigenvector orientation as assessed by the DTI model.

Figure 5. Zeppelin-sphere model parameter maps.

Slice positions as for Figs. 1&2. Parameter maps for the Tensor-sphere model for the same slices are provided in Supporting Figure S1. For reference the Ball *D* (ADC) parameter maps are included.

Figure 6. Two-way parameter histograms for Zeppelin-sphere model.

Pixel brightness proportional to voxel count. Note that when a component's signal fraction is low the parameter estimates for that component may be unreliable. The majority of voxels in each of the four prostates have biophysically plausible parameter values.

Figure S1. Tensor-sphere model parameter maps.

Slice positions as for Figs. 1&2.

Figure S2. One-way parameter histograms for Zeppelin-sphere model.

Table S1. *P*-values from Mann-Whitney U-test.

Insignificant differences ($P > 0.05$) between models are shown in bold type.
1 – Ball, 2 – Bi-ball, 3 – Ball-zeppelin, 4 – Bi-ball-zeppelin, 5 – Zeppelin-sphere,
6 – Bi-zeppelin, 7 – Tensor-sphere, 8 – Ball-sphere, 9 – Ball-tensor, 10 – DTI

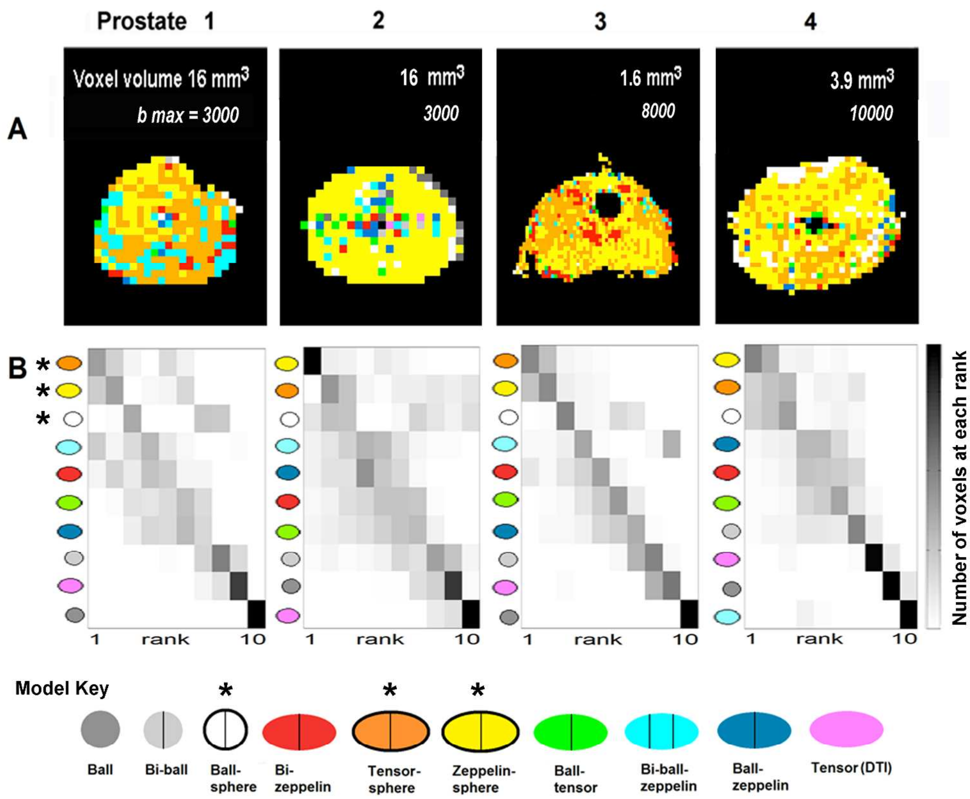

Figure 1. Variation of model rankings in four prostates.
A) Anatomical distribution of the highest ranked model in a mid-organ slice from each prostate. (See Fig. 2 for pathology maps of these slices). Voxel color indicates model according to the Model key. The Zeppelin-sphere (yellow) or Tensor-sphere (orange) models ranked highest in most voxels in all prostates.
B) Variation of model rank positions. The grey scale indicates the number of times each model ranked at each position (eg. the Ball model ranked 10th in nearly all voxels). The model order (vertically) is based on trends assessed subjectively. See Fig. 3 for statistical summary of AIC ranks.
Data from 558 voxels from slices 5&6 in Prostate 1, 504 voxels from slices 5&6 in Prostate 2, 1278 voxels from slices 7-9 in Prostate 3, and 2041 voxels from slices 3-6 in Prostate 4.
Model Key: The three models containing a restricted component are shown with a heavy black border. Models with an anisotropic component are shown as ellipses. Vertical lines indicate number of components. Models including a restricted component are marked with an asterisk.

260x224mm (300 x 300 DPI)

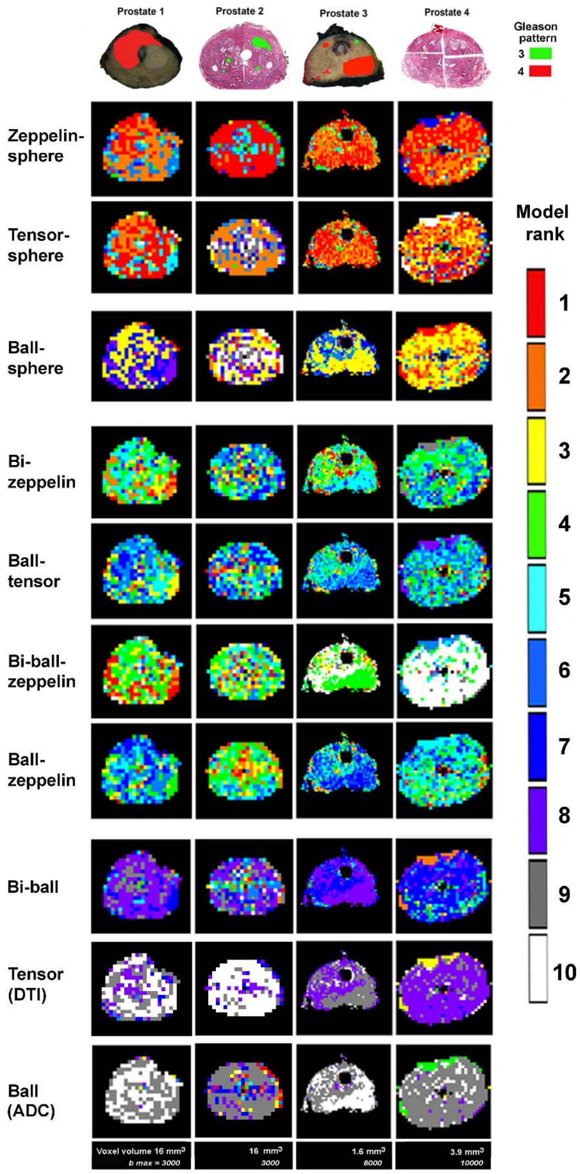

Figure 2. Variation in rankings of individual models in four prostates.
Slice positions as for Figs 1 and 5. Voxel color indicates model rank and models are grouped according to predominant rank.

224x445mm (300 x 300 DPI)

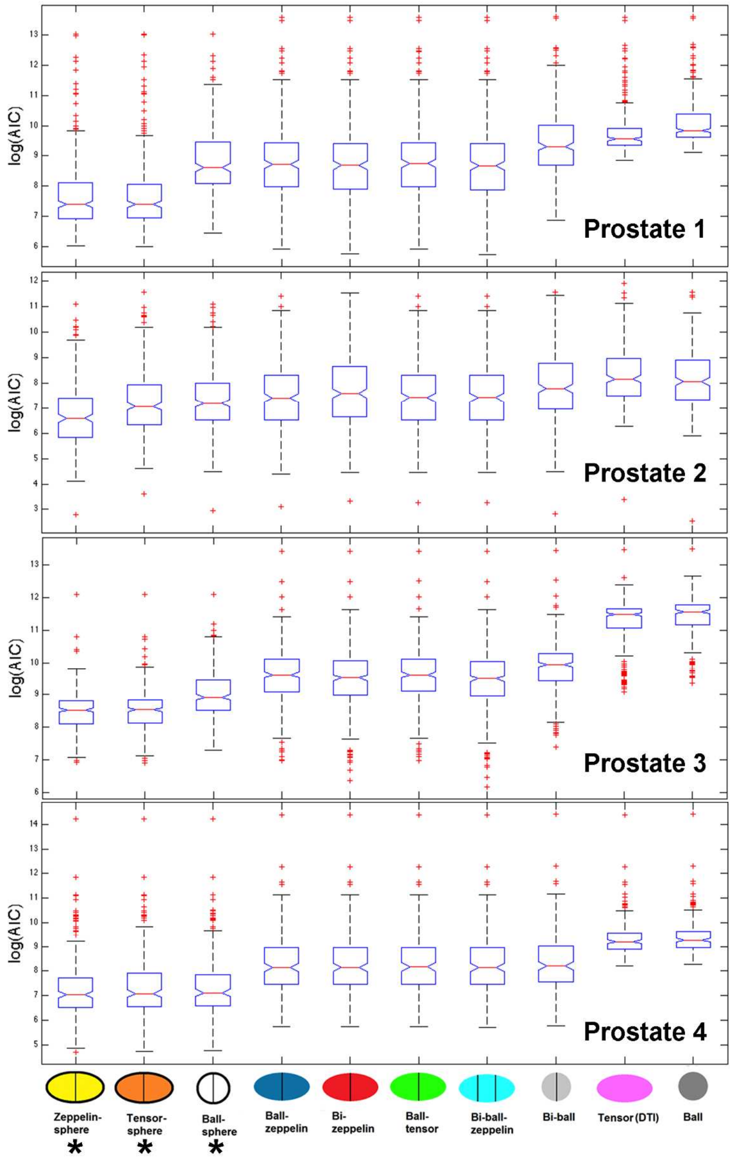

Figure 3. Box and whiskers plots of log(AIC).
Models including a restricted component are marked with a black asterisk. For each blue box, the central red mark is the median and the top and bottom edges of the box are the 25th and 75th percentiles. The whiskers extend to the most extreme data points that are not considered outliers. Outliers are plotted individually in red.
Distributions were normal after the log transformation. Data from 558 voxels from slices 5&6 in Prostate 1, 504 voxels from slices 5&6 in Prostate 2, 1278 voxels from slices 7-9 in Prostate 3, and 2041 voxels from slices 3-6 in Prostate 4. Results for Mann-Whitney U-test are presented in Supplementary Material available online.

149x230mm (300 x 300 DPI)

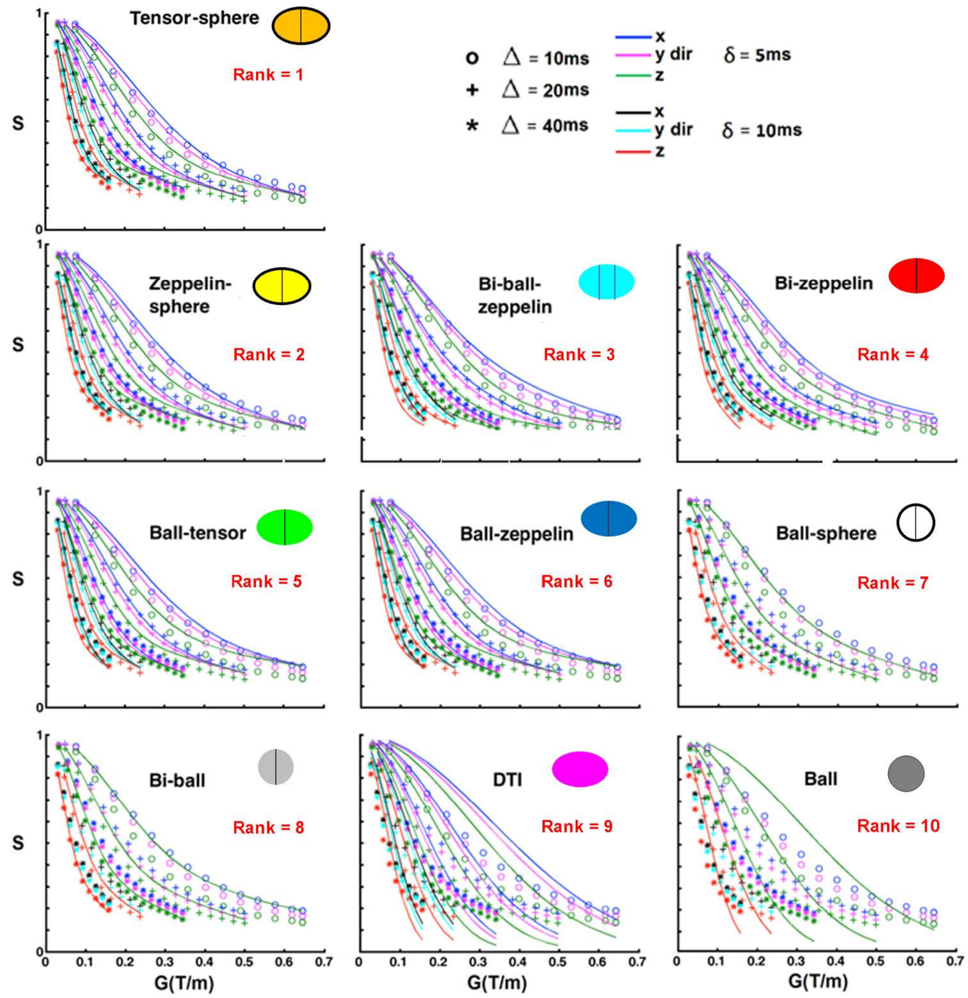

Figure 4. Representative model fit data.
Measurement data (symbols) and model fit (lines). Normalized signal *S* is plotted for all values of Δ and δ as a function of gradient strength |G| for x, y, z directions. Indicated model rank is specific to this data set. Measurement data (SNR ~600) is the average from four adjacent 1×0.78×2 mm^3 voxels in the transition zone of Prostate 3 with similar primary eigenvector orientation as assessed by the DTI model.

240x250mm (300 x 300 DPI)

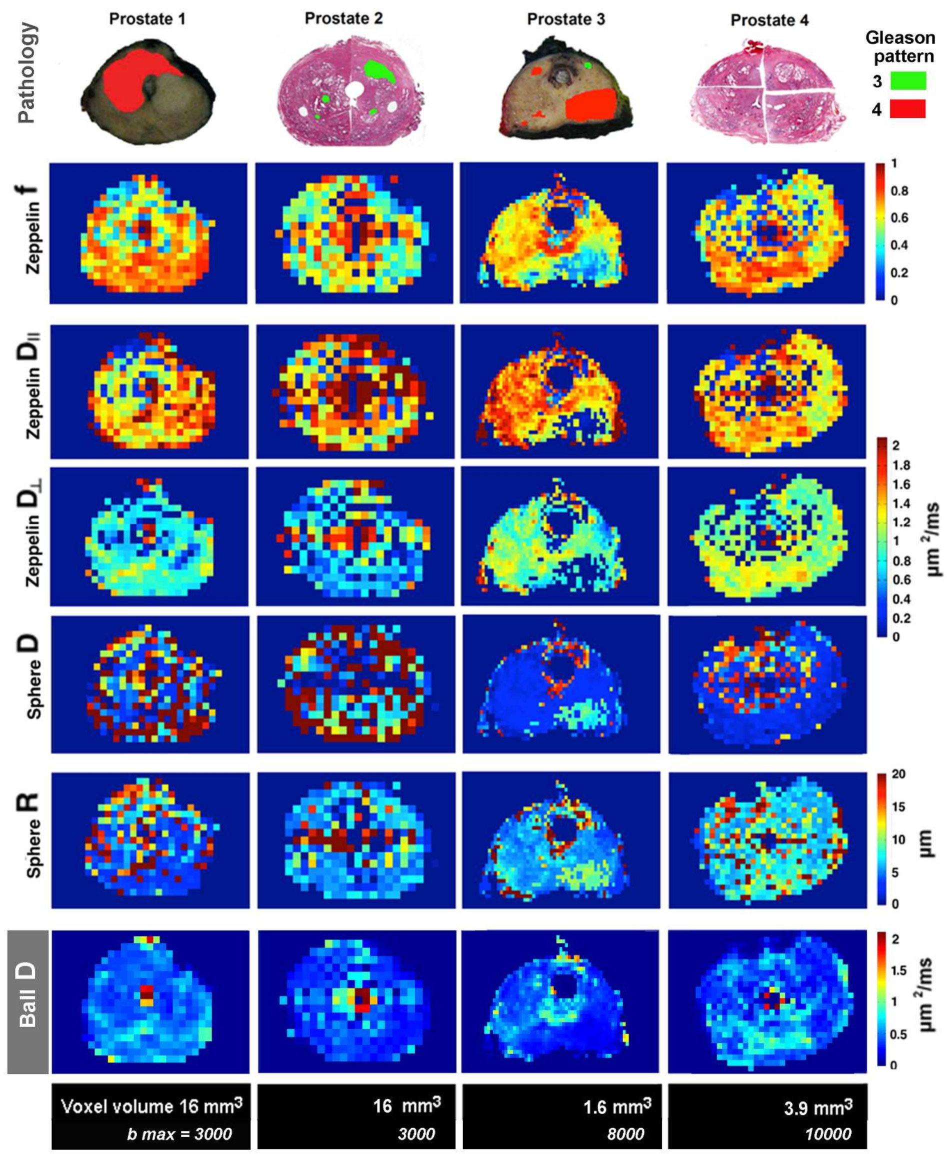

Figure 5. Zeppelin-sphere model parameter maps.
Slice positions as for Figs. 1&2. Parameter maps for the Tensor-sphere model for the same slices are provided in Supporting Figure S1. For reference the Ball *D* (ADC) parameter maps are included.

223x277mm (300 x 300 DPI)

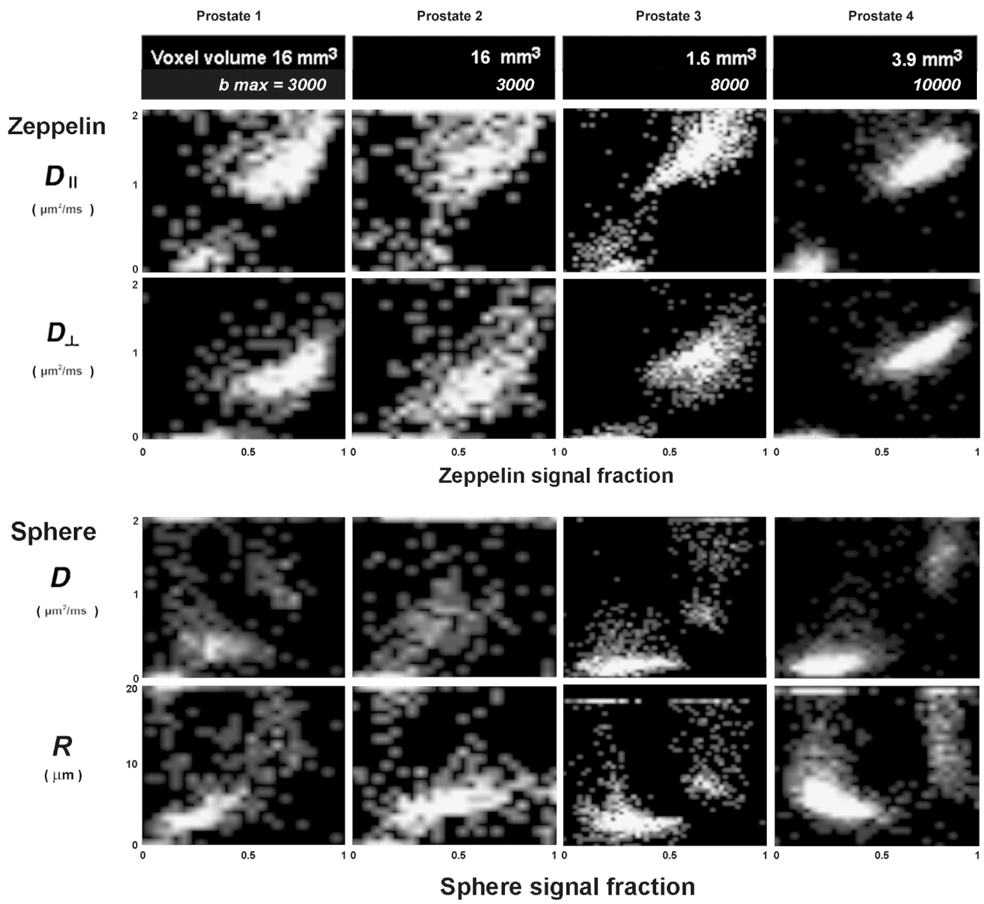

Figure 6. Two-way parameter histograms for Zeppelin-sphere model.
Pixel brightness proportional to voxel count. Note that when a component's signal fraction is low the parameter estimates for that component may be unreliable. The majority of voxels in each of the four prostates have biophysically plausible parameter values.

236x215mm (300 x 300 DPI)

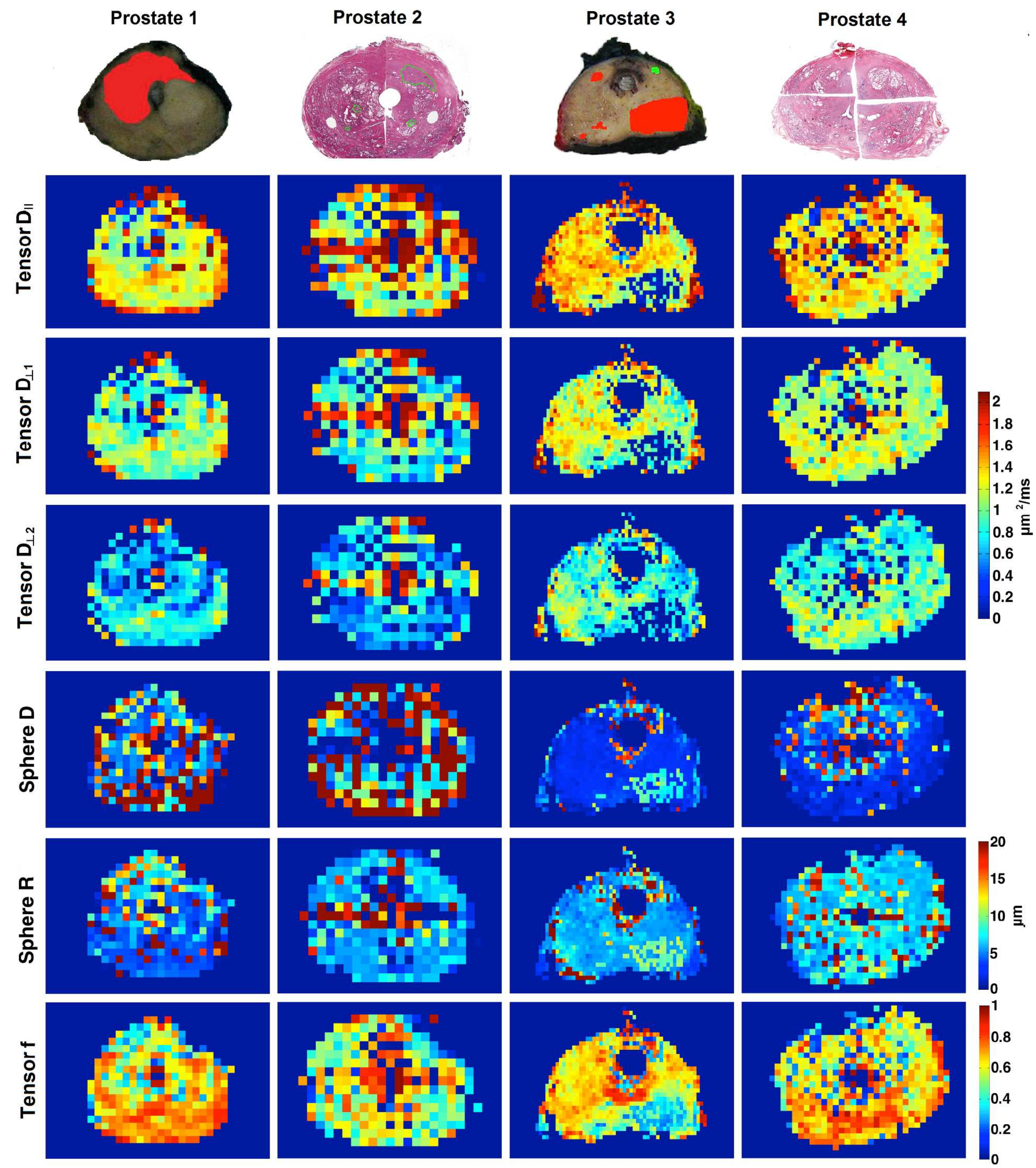

Figure S1. Tensor-sphere model parameter maps.

Slice positions as for Figs. 1&2.

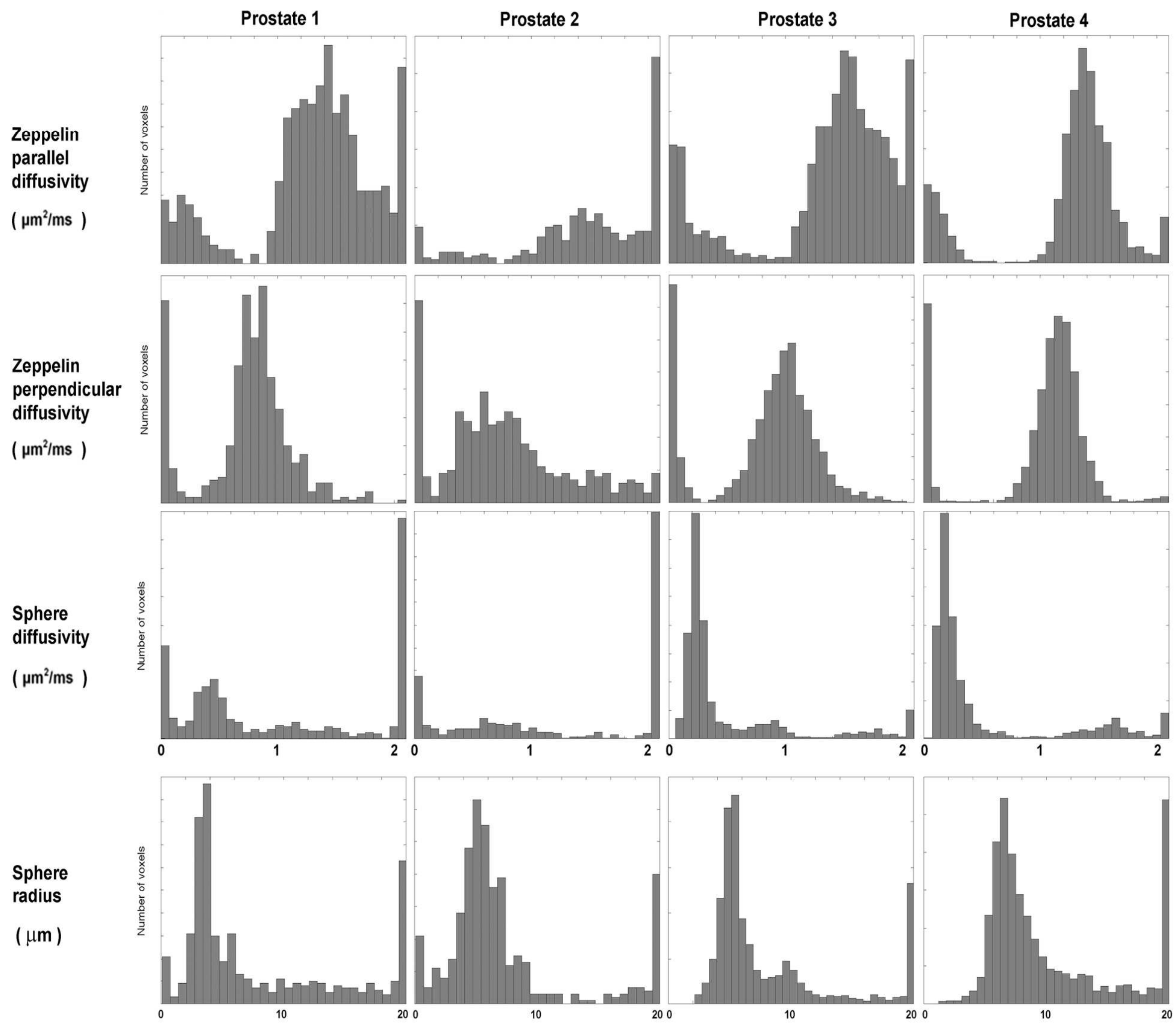

Figure S2. One-way parameter histograms for Zeppelin-sphere model.

Table S1. *P*-values from Mann-Whitney U-test.

Insignificant differences ($P > 0.05$) between models are shown in bold type.
1 – Ball, 2 – Bi-ball, 3 – Ball-zeppelin, 4 – Bi-ball-zeppelin, 5 – Zeppelin-sphere, 6 – Bi-zeppelin, 7 – Tensor-sphere, 8 – Ball-sphere, 9 – Ball-tensor, 10 – DTI

Prostate 1

	2	3	4	5	6	7	8	9	10
1	4×10^{-21}	2×10^{-45}	6×10^{-46}	2×10^{-75}	8×10^{-46}	3×10^{-74}	2×10^{-49}	7×10^{-45}	5×10^{-16}
2		6×10^{-12}	3×10^{-13}	2×10^{-56}	5×10^{-13}	1×10^{-55}	2×10^{-13}	1×10^{-11}	7×10^{-8}
3			**0.48**	2×10^{-33}	**0.54**	1×10^{-32}	**0.78**	**0.89**	4×10^{-33}
4				6×10^{-29}	**0.89**	3×10^{-28}	**0.7**	**0.39**	7×10^{-34}
5					2×10^{-29}	**0.9**	3×10^{-33}	7×10^{-34}	3×10^{-70}
6						6×10^{-29}	**0.78**	**0.45**	9×10^{-34}
7							1×10^{-32}	3×10^{-33}	1×10^{-68}
8								**0.68**	2×10^{-35}
9									1×10^{-32}

Prostate 2

	2	3	4	5	6	7	8	9	10
1	**0.01**	3×10^{-11}	2×10^{-11}	2×10^{-35}	1×10^{-5}	2×10^{-19}	7×10^{-17}	3×10^{-11}	**0.38**
2		9×10^{-5}	7×10^{-5}	1×10^{-23}	**0.06**	5×10^{-10}	3×10^{-8}	9×10^{-5}	4×10^{-4}
3			**0.95**	2×10^{-11}	**0.06**	0.02	**0.11**	**0.93**	4×10^{-14}
4				3×10^{-11}	**0.05**	0.02	**0.13**	**0.89**	3×10^{-14}
5					8×10^{-16}	3×10^{-6}	7×10^{-8}	1×10^{-11}	1×10^{-39}
6						4×10^{-5}	7×10^{-4}	0.07	1×10^{-7}
7							**0.41**	0.01	2×10^{-23}
8								**0.1**	1×10^{-20}
9									4×10^{-14}

Prostate 3

	2	3	4	5	6	7	8	9	10
1	1×10^{-87}	1×10^{-95}	5×10^{-97}	4×10^{-112}	7×10^{-97}	1×10^{-111}	1×10^{-107}	1×10^{-95}	1×10^{-4}
2		4×10^{-7}	6×10^{-11}	4×10^{-80}	3×10^{-10}	3×10^{-76}	1×10^{-40}	4×10^{-7}	2×10^{-80}
3			**0.99**	4×10^{-60}	**0.14**	1×10^{-56}	8×10^{-21}	**0.99**	2×10^{-89}
4				1×10^{-48}	**0.71**	1×10^{-45}	8×10^{-14}	**0.08**	2×10^{-91}
5					3×10^{-51}	**0.69**	5×10^{-22}	5×10^{-60}	3×10^{-111}
6						5×10^{-48}	4×10^{-15}	**0.15**	4×10^{-91}
7							4×10^{-20}	1×10^{-56}	1×10^{-110}
8								9×10^{-21}	4×10^{-104}
9									2×10^{-89}

Prostate 4

	2	3	4	5	6	7	8	9	10
1	4×10^{-22}	4×10^{-23}	3×10^{-23}	6×10^{-40}	4×10^{-23}	4×10^{-39}	1×10^{-39}	4×10^{-23}	**0.21**
2		**0.55**	**0.47**	3×10^{-17}	**0.51**	3×10^{-15}	5×10^{-15}	**0.59**	2×10^{-20}
3			**0.85**	2×10^{-15}	**0.92**	1×10^{-13}	3×10^{-13}	**0.99**	1×10^{-21}
4				1×10^{-14}	**0.91**	5×10^{-13}	1×10^{-12}	**0.82**	1×10^{-21}
5					4×10^{-15}	**0.52**	**0.25**	1×10^{-15}	2×10^{-39}
6						2×10^{-13}	6×10^{-13}	**0.9**	1×10^{-21}
7							**0.63**	7×10^{-14}	2×10^{-38}
8								2×10^{-13}	5×10^{-39}
9									1×10^{-21}

Information based ranking of ten compartment models of diffusion weighted signal attenuation in fixed prostate tissue.

Sisi Liang, Eleftheria Panagiotaki, Andre Bongers, Peng Shi, Paul Sved, Geoffrey Watson, Roger Bourne*

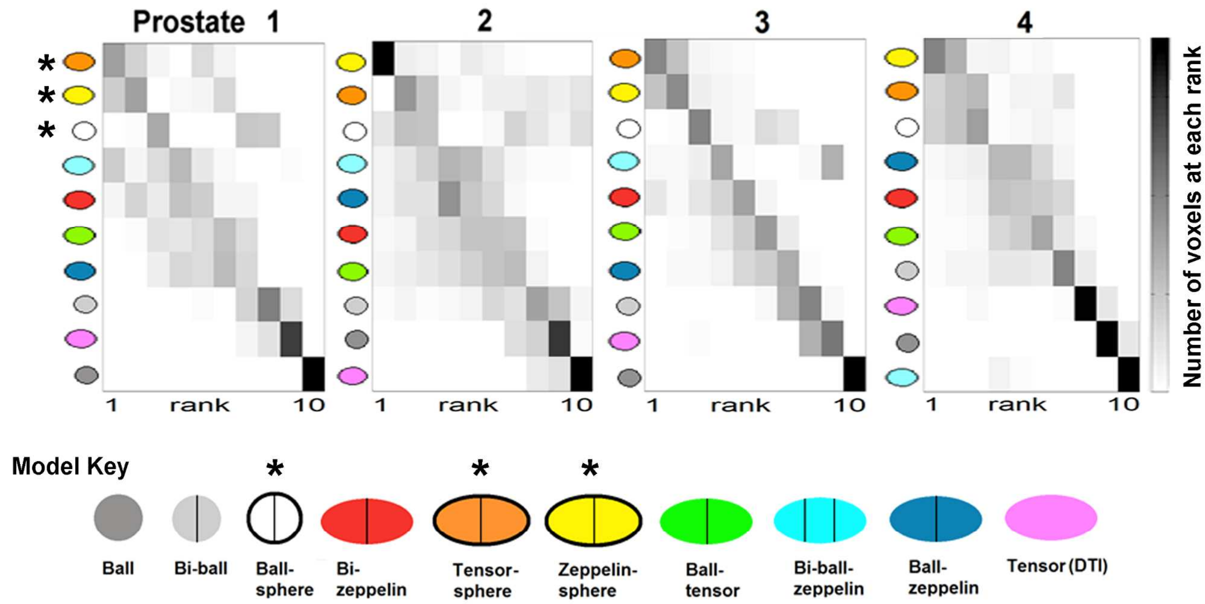

In all four prostates either the Zeppelin-sphere or Tensor-sphere model was ranked highest in the large majority of voxels. The results suggest that both anisotropic and restricted components are required to accurately describe DWI signals measured over an extended range of *b*-values and multiple diffusion times.

Information based ranking of ten compartment models of diffusion weighted signal attenuation in fixed prostate tissue.

Authors:

Sisi Liang — College of Engineering and Science, Victoria University, Melbourne, Australia

Eleftheria Panagiotaki — Center for Medical Image Computing, University College London, London, UK

Andre Bongers — Mark Wainright Analytical Centre, University of New South Wales, Sydney, Australia

Peng Shi — College of Engineering and Science, Victoria University, Melbourne, Australia

Paul Sved — Department of Urology, Royal Prince Alfred Hospital, School of medicine, University of Sydney, Sydney, Australia

Geoffrey Watson — Department of Tissue Pathology and Diagnostic Oncology, Royal Prince Alfred Hospital, Sydney, Australia

Roger Bourne — Discipline of Medical Radiation Sciences, Faculty of Health Sciences, University of Sydney, Sydney, Australia

Correspondence:

Roger Bourne,

Discipline of Medical Radiation Sciences, Faculty of Health Sciences,

UNIVERSITY OF SYDNEY, 75 East Street, Lidcombe, NSW, 2141, Australia

Tel: +61 2 9036 7350 Fax: +61 2 9351 9146

e: roger.bourne@sydney.edu.au

Running head:

Ten models of diffusion in prostate tissue

Key words:

Diffusion; prostate; modeling; compartment models; restricted diffusion; microstructure imaging

Word count: 3442

Abbreviations used: ADC, apparent diffusion coefficient; AIC, Akaike Information Criterion; DWI, diffusion weighted imaging; SNR, signal-to-noise ratio; DCE, dynamic contrast enhanced; mpMRI, Multiparametric MRI; DTI, diffusion tensor imaging; FA, fractional anisotropy; MD, mean diffusivity;

Title

Information based ranking of ten compartment models of diffusion weighted signal attenuation in fixed prostate tissue.

Sisi Liang, Eleftheria Panagiotaki, Andre Bongers, Peng Shi, Paul Sved, Geoffrey Watson, Roger Bourne

Abstract

This study compares the theoretical information content of single and multi-compartment models of diffusion weighted signal attenuation in prostate tissue. Diffusion weighted imaging (DWI) was performed at 9.4T with multiple diffusion times and an extended range of *b*-values in four whole formalin fixed prostates. Ten models, including different combinations of isotropic, anisotropic, and restricted components were tested. Models were ranked using Akaike's Information Criterion. In all four prostates two-component models comprising an anisotropic Gaussian component and an isotropic restricted component ranked highest in the majority of voxels. Single component models, whether isotropic (ADC) or anisotropic (DTI), consistently ranked lower than multicomponent models. Model ranking trends were independent of voxel size and maximum *b*-value in the range tested (1.6-16 mm^3 and 3000-10,000 s/mm^2). This study characterizes the two major water components previously identified by biexponential models and shows that models incorporating both anisotropic and restricted components provide more information-rich descriptions of DWI signals in prostate tissue than single or multicomponent anisotropic models and models that do not account for restricted diffusion.

Key words: diffusion; prostate; modeling; compartment models; restricted diffusion; microstructure imaging

Introduction

At present the optimum choice of therapy for prostate cancer, and even whether therapy is warranted, remains unclear and controversial. While it is well established that the best indicator of cancer aggressiveness is the grade and volume of cancer, at present this can only be measured reliably after removal of the prostate (1-3). Multiparametric MRI (mpMRI) combining T_2-weighted, dynamic contrast enhanced (DCE), and diffusion weighted imaging (DWI) is increasingly being used to assist targeted biopsy, risk stratification, and treatment selection for prostate cancer (4-6). The sensitivity and specificity of the three methods combined is usually higher than for any one method alone, however, DWI shows stronger correlations with both cancer grade and volume than T_2 and DCE (7-9).

The superior cancer detection performance of DWI is remarkable because the standard method – calculation of an apparent diffusion coefficient (ADC) using a monoexponential signal model – is highly simplistic and assumes a Gaussian spin displacement behavior that is well known to be invalid in biological tissue (10). The success of simple ADC-based prostate cancer detection can be attributed to the direct relationship between DWI signal attenuation and the tissue microstructural features that define the presence and grade of cancer (11), and suggests that more sophisticated DWI acquisitions and signal analysis methods are likely to significantly improve the performance of mpMRI. Phenomenological approaches have demonstrated that DWI measurements over an extended range of *b*-values are inherently more information-rich than an ADC model would suggest (12,13), and may provide more accurate detection of prostate cancer in clinical prostate imaging (14-16). However, in general, phenomenological models of measured signals do not provide parameter values that can be directly related to tissue structure properties.

Ideally, models for cancer assessment would be based on tissue microstructure. To this end, a three-component 'VERDICT' model based on vascular, extravascular/extracellular, and intracellular compartments has recently been shown to provide more reliable discrimination of cancer and normal tissue than monoexponential and biexponential signal models, and to return model parameters consistent with histological features such as average cell diameter (17). A significant innovation of VERDICT is the inclusion of a restricted diffusion component (the putative intracellular compartment), the fitting of which requires DWI signal acquisition at multiple diffusion times.

Previous prostate studies utilizing the VERDICT framework in a clinical setting (18,19) used only isotropic compartment models. A recent study of diffusion anisotropy in prostate tissue using a conventional diffusion tensor imaging (DTI) model reported wide variations in mean voxel fractional anisotropy (FA) between prostates and a strong voxel size dependency with FA decreasing as voxel size increases (20). Diffusion microimaging of fixed prostate tissue demonstrates high anisotropy in the fibromuscular stroma and low FA in the glandular epithelium and lumen spaces (21). A typical clinical DWI sized voxel (volume 4-16 mm^3) is likely to contain a mixture of isotropic and anisotropic compartments. A single component DTI model will have limited ability to detect the actual anisotropy of the stromal component if the partial volumes of epithelium and lumen space are significant. Multi-compartment models that include at least one anisotropic component would be expected to provide a more precise description of such sub-voxel heterogeneity than DTI and isotropic models.

In the study presented here we investigate the relative information content of compartment models that include anisotropic components and test the importance of inclusion of a restricted diffusion compartment. To obtain 'ground truth' data to inform the further development of clinical imaging methods we performed these studies in the absence of perfusion effects using radical prostatectomy specimens and high signal-to-noise ratio (SNR) measurements which enable model fitting with fewer parameter constraints than in previous applications of the VERDICT model.

Methods

Tissue Handling and Histopathology

The study was conducted with institutional ethics approval and written informed consent from all patients. Four whole prostates were imaged: Prostate 1, age 59y, 47g, Gleason 4+4; Prostate 2, age 57y, 38g, Gleason 3+3; Prostate 3, 56y, 47g, Gleason 3+4; Prostate 4, normal prostate, 35g, from cystoprostatectomy for bladder cancer. The intact organ was sent to the pathology department immediately upon surgical resection and without immersion in a fixative solution. The organ was weighed and inked and the seminal vesicles and any surgical clips were removed prior to transport and imaging of the unfixed tissue (for investigations not reported here). The total time between resection and immersion in formalin was 6-8 hr. A specialist urological pathologist confirmed no significant tissue degradation due to delayed fixation of the specimens. Following immersion in 10% neutral buffered formalin for 24 hr, the fixed prostate was soaked in saline for 24 hr before imaging for 24-48 hr and then returned to the hospital pathology department for routine processing. Prostates were sectioned at 4-mm intervals in planes orthogonal to a tube inserted through the urethra and parallel to the imaging slices (see below). All the measurements reported here were performed on the fixed specimens.

MR Imaging

Prostates 1 and 2 were scanned with nominal *b*-value range 50-3000 s/mm^2 and voxel size 2×2×4 mm^3 to emulate feasible clinical voxel sizes and *b*-values. Prostates 3 and 4 were imaged at high spatial resolution (voxel size 1×0.78×2 mm^3 and 1.4×1.4×2 mm^3 respectively) over an extended *b*-value range of 50-10354 s/mm^2. The use of a range of acquisition parameters tests the generality of the model selection and intentionally includes protocols feasible in clinical scanners together with methods only possible with high gradients and ex vivo samples. The range of voxel sizes used tests for any effect of variation in subvoxel tissue heterogeneity.

Each organ was imaged suspended on a 5-mm saline-filled NMR tube inserted through the urethra and mounted in brackets in a plastic casing that maintained the tube axis parallel to and approximately 5 mm above the magnet Z-axis (22). Imaging was performed at room temperature (22°C) on a 9.4T Bruker (Bruker, Karlsruhe, Germany) BioSpec Avance III 94/20 magnetic resonance microimaging system equipped with a 72-mm internal diameter quadrature radiofrequency coil and BGA-12S HP gradients with maximum strength 660 mT/m and slew rate 4570 T/m/s. Imaging was performed transaxial to the urethra with the imaging planes oriented orthogonal to the 5-mm NMR tube. A paint landmark was used to identify the central imaging plane for later sectioning of the organ (see above).

For all prostates, diffusion encoding used a pulse-gradient spin-echo method with three orthogonal diffusion encoding gradient directions. All diffusion weighted measurements were preceded by the acquisition of two reference '*b* = 0' images. Intrinsic SNR was calculated from a large intraprostatic region of interest in a pair of reference images (23). Additional DTI acquisitions were performed using a 6-direction scheme. DWI and DTI acquisition parameters are detailed in Table 1.

Model Description

Models with one to three compartments were tested with components described according to the taxonomy used for brain tissue DWI in (24). The individual components (Table 2) that were combined to create the multi-compartment models included: 1) a conventional single-component DTI model, which provides two commonly used summary parameters FA and mean diffusivity (MD) (25); 2) a Zeppelin, which is a cylindrically symmetric tensor that also provides FA and MD; 3) a Ball which is an isotropic tensor; and 4) as in (17), a Sphere compartment describing restricted diffusion within a non-zero radius spherical pore. Each model compartment was fitted individually and in a variety of combinations to test and evaluate in total ten models (Table 3).

Model Fitting

A wide range of imaging parameters was used to ensure stable fitting (17). DWI measurements included 3-direction data with multiple b-values and multiple Δ and δ values, combined with single b-value and single δ/Δ-value 6-direction data to enable fitting of anisotropic components. The acquisition of data at multiple diffusion times enables estimation of a restriction radius based on the diffusion time dependence of the apparent diffusion coefficient. Each model was fitted to the combined 3- and 6-direction data using the Levenberg-Marquardt minimization algorithm in the open source Camino toolkit (26). To minimize any possible T_2 effects data were normalized to the 'b=0' signal prior to fitting (17). Model fitting was based on minimization of an objective function that uses an offset-Gaussian noise model to account for the inherent Rician distributed noise in the magnitude MRI data (17). Model parameters were constrained within meaningful biophysical limits. Radius R of the isotropic restricted 'sphere' component was constrained to the range 0.1-20 μm according to typical cell diameter. All component signal fractions were constrained to a range of 0-1 and sum to 1. Diffusivities were constrained so that $0 \leq D \leq 2.1$ μm^2/ms according to the 22^{o}C sample temperature (27).

Model Ranking

Models were ranked using the Akaike Information Criterion (AIC) which compares models in terms of theoretical information content (28). AIC provides an estimate of the relative distance of competing models from the (usually unknowable) system truth and avoids the use of arbitrary cutoffs required for hypothesis testing. In prostate tissue AIC-based model ranking has previously been shown to be consistent with a leave-one-out test of model prediction accuracy (12,13). Differences between model ranking AIC scores were assessed via a Mann-Whitney U-Test performed in Matlab.

Results

Figure 1 summarizes variation in model rankings based on AIC and shows the anatomical distribution of the highest ranked models in a mid-organ transverse slice of each prostate. Figure 2 shows the rank variations of the individual models, and Fig. 3 provides box and whiskers plots of the variation in AIC scores within and between models for each prostate. Log(AIC) data is presented in Fig. 3 as this produced a normal distribution of the skewed raw AIC scores.

In all four prostates either the Zeppelin-sphere or Tensor-sphere model was ranked highest in the large majority of voxels. There was no distinct variation of ranking according to prostate zonal anatomy (not assessed quantitatively). The differences between eigenvalues of the Tensor and Zeppelin components of these models were minor (data not shown). The only other model that included a restricted component, the Ball-sphere, ranked close to Zeppelin-sphere and Tensor-sphere. The single component Ball (ADC) and DTI models ranked low in all prostates. In general, multi-component models that included one or two anisotropic components ranked higher than models that did not account for anisotropy, and models that included a restricted diffusion compartment ranked higher than those that did not. Model ranking trends were largely independent of voxel size, maximum b-value, maximum diffusion time, and whether or not two different diffusion encoding pulse lengths (δ) were used (Table 1).

Results of a Mann-Whitney U-test for significant differences between AIC scores are presented in the supplementary material available online. The statistical analysis shows that the AIC ranking suggests three primary groups: 1) Zeppelin-sphere, (Tensor-sphere); 2) Ball-zeppelin, (Ball-sphere), Bi-ball-zeppelin, Bi-zeppelin, Ball-tensor; 3) Ball, (Bi-ball), DTI. The brackets indicate models that may appear in other group in some prostates. The Group 1 models have significantly lower AIC scores than Group 2 and 3 models, consistent with the qualitative data presented in Figs 1 and 2.

These results indicate that two-component Zeppelin-sphere and Tensor-sphere models that account for both anisotropy and diffusion restriction provide more information-rich descriptions of multi-Δ, multi-*b* DWI measurement data than simpler isotropic, DTI, and unrestricted models.

Figure 4 provides a visual illustration the fit of the ten models to summed data from a homogeneously anisotropic four-voxel region of interest in normal transition zone tissue. Although the DTI-estimated anisotropy of the four voxels was low (range 0.17-0.20) the highest six AIC-ranked models all include at least one anisotropic component and provide better fits to the measurement data than the isotropic models and the single component DTI model. Nevertheless, it is also evident that not even the most highly parameterized models provide an exact description of the measurement data, indicating signal modulation effects that these models do not capture.

Parametric maps derived from the Zeppelin-sphere model are presented in Figure 5 together with mapped pathology from approximately the same slice location. The Ball-*D* parameter map (ADC) is included for reference. Very similar parameter maps were obtained for the Tensor-sphere model (Supporting Figure S1).

Parameter histogram images for the Zeppelin-sphere model are shown in Figure 6. The histograms are presented as *D* or *R* versus component signal fraction. When the component signal fraction is low the bias and variance for that component's parameters would be expected to be higher than when the signal fraction (and hence the component SNR) is high. In the majority of voxels the diffusivity parameter values are biophysically plausible (less than the diffusion coefficient for pure water at 22^{o}C (29)). The sphere radius parameter value range (Fig. 6) is also consistent with typical cell diameters. Simple histograms of *D* and *R* are provided in Supplementary Figure S2.

Discussion

This study extends previous comparisons of phenomenological isotropic single and two component models of DWI signals measured ex vivo in prostate tissue. Bourne et al. (12) found that for measurements including *b*-values above 2000 s/mm^2 (at δ/Δ = 5/20 ms) a biexponential model had a higher information content than monoexponential (ADC), stretched exponential, and kurtosis models. Hall et al. (13) examined the value of the stretched exponential as a modifier of the 'slow' and 'fast' components of the biexponential model, demonstrating that at all diffusion times tested (8, 18, and 38 ms) the 'slow' water pool exhibits distinctly non-Gaussian displacement dynamics. The 'fast' water pool tended towards Gaussian behavior at the longer diffusion times. Whilst those studies clearly demonstrate the presence of two distinct spin pools, a limitation was the lack of modeling of diffusion anisotropy and restricted diffusion. The 'slow' non-Gaussian water pool described by Hall et al. most probably corresponds to the restricted sphere component of our models, and the 'fast' component to our anisotropic component.

The study presented here suggests that both anisotropic and restricted components are required to accurately describe DWI signals measured over an extended range of *b*-values and multiple diffusion times. The consistentently high ranking of the anisotropic+restricted two component models over a range of voxel sizes strongly suggests that the spin pools represented by the two components exist on a microscopic scale and that any tissue heterogeneity on a mesoscopic scale (for example variations in gland density) does not produce significant partial volume effects for the voxel sizes measured in this study.

Our results are consistent with Bourne et al. (12) and Hall et al. (13) in demonstrating the relatively poor performance of single component (ADC/Ball and DTI) models and the isotropic biexponential (Bi-ball) model. It is noteworthy that to date ADC and DTI models have been the most commonly used analysis of in vivo prostate DWI measurements, and that ADC is a cornerstone of the mpMRI-based prostate cancer assessment protocol (4-6). The low AIC ranking of ADC and DTI models in this study suggests that the performance of DWI in prostate cancer assessment might be improved by implementation of more sophisticated DWI protocols such as the three-component structure-based 'VERDICT' model (18).

Comparison with VERDICT model

VERDICT (18) has been utilized to quantify and map histological features of prostate tissue based on in vivo multi-Δ, multi-b DWI measurements. The results suggest VERDICT can discriminate benign and cancerous tissue better than ADC (Ball), kurtosis, and biexponential (Bi-ball, or intravascular incoherent motion (30)) models. The three components of the VERDICT model are based on vascular, extravascular/extracellular, and intracellular compartments. The prostate-specific form of the generic VERDICT model is designed to account for: 1) water trapped in cells (modeled as a sphere component); 2) interstitial water (modeled as an isotropic diffusion tensor); and 3) water in the vasculature (modeled as restricted water in cylinders with uniformly distributed orientations and zero diameter) (18,19). Our study of unperfused prostate tissue ex vivo provides further information about the 'true diffusion' (non-perfusion) components of the VERDICT model, and in particular demonstrates the presence of a significant anisotropic diffusion component.

An important difference between our model fitting strategy and VERDICT is the number of fitted parameters. The large number of b-values and high SNR of our measurements enabled the reliable (low parameter variance) fitting of more highly parameterized models with fewer constraints on parameter values. When applying the VERDICT model to in vivo prostate data all component diffusivities (including the pseudodiffusion coefficient of the vascular component) were fixed to values previously found to minimize an objective function ('fitting error') over all voxels (18), all three components were isotropic, and only three independent parameters were fitted (intravascular volume fraction, extracellular extravascular volume fraction, and sphere radius). These constraints were necessary to avoid overfitting of the relatively noisy in vivo data.

In contrast to in vivo prostate VERDICT model fitting we permitted all diffusion coefficients to float within biophysical limits and allowed for diffusion anisotropy with the Tensor and Zeppelin components. In the large majority of voxels the fitting returned parameter values inside the defined limits, a strong indication that the models are biophysically plausible. The superior AIC performance of the minimally constrained multi-component anisotropic and restricted diffusion models over the isotropic, unrestricted, and single component anisotropic models indicates that the parameter values of these less constrained models contain information about the tissue microstructure.

When applying the VERDICT model to in vivo prostate DWI data, Panagiotaki et al. constrained the 'true' diffusivity parameters (intracellular water and extracellular extravascular water) to a fixed value of 2 $\mu m^2/ms$ (18), which corresponds to ~1.4 $\mu m^2/ms$ at 22°C (27). The value of 1.4 $\mu m^2/ms$ is consistent with the main peaks in the Zeppelin diffusivity histograms of our data (Fig. 6).

The high ranking of the Tensor-sphere, Zeppelin-sphere, and Ball-sphere models in the majority of voxels in all four prostates, even in the absence of fixed diffusivity parameter values, indicates the importance of accounting for restricted diffusion in any modeling of prostate tissue and supports the inclusion of a restricted component in VERDICT.

Cancer detection

Our study demonstrates that for DWI measurements over an extended *b*-value range and including multiple diffusion times the anisotropic/restricted diffusion models have higher theoretical information content than conventional ADC and DTI models. Nevertheless, it should be noted that it is possible that this information does not have any extra value for identification of pathology. The small number of prostates included in this study precludes a quantitative assessment of the value of the tested models for cancer detection. The information-based ranking of models we applied balances the tradeoff between parameter bias and variance, and *predicts* the relative ability of models to explain measurement data (28). While many published studies compare the cancer detection performance of different DWI signal models in terms of correlation of individual model parameters with tissue pathology this approach neglects the possibility that the pathology-specific (diagnostic) information is distributed between two or more model parameters (12,31). Whatever signal model is employed, it is also possible that the imaging method (eg. diffusion times, *b*-values, gradient orientations) does not provide appropriate data for pathology discrimination. Information theory defines the most likely useful model(s), the pathology detection performance of which should then be assessed by correlation of single and combined parameters with accurately matched pathology data from a large number of samples.

Limitations

This study has several limitations. Imaging of the tissue ex vivo enables acquisition of high spatial resolution high SNR data free from movement and other artifacts, and free from perfusion effects, but the absence of perfusion may result in a decreased volume of extravascular extracellular water which would be expected to have some effect on the signal fractions for each compartment.

Formalin fixation stabilizes the tissue against degradation by cross-linking of protein but consequently leads to a decrease in measured tissue diffusivities (22,32). Previous studies suggest this is unlikely to affect model ranking (12,33).

To maximize SNR we used the minimum available echo time for each diffusion time and normalized the measurements to the maximum (‘$b = 0$’) signal to minimize any effects of T_2 heterogeneity. While there is some evidence for the existence of sub-voxel T_2 heterogeneity in prostate tissue (34,35), it is not clear that the apparently distinct T_2 water pools correspond to the two main water pools identified in multi-*b* DWI studies. This is an important topic for future investigation.

The models we tested assumed no exchange of water between compartments. To our knowledge exchange has yet to be investigated in prostate tissue. Having defined relatively simple models, such as Zeppelin-sphere, that appear to provide robust descriptions of rich data such as we acquired in these experiments, a logical next step would be to assess the value of accounting for exchange between the two compartments.

The differences between our 9.4T ex vivo measurement conditions and in vivo imaging include temperature, perfusion, tissue fixation, *b*-value range, diffusion time range, available diffusion encoding gradient strength, echo time, and SNR. Although our results cannot be directly related to in vivo prostate imaging they define some of the tissue structure properties that can be detected by DWI and emphasize a significant potential of DWI that goes currently unrealized in simple ADC and DTI techniques. The results provide basic science evidence to guide the further development of promising compartment models such as VERDICT.

CONCLUSIONS

When DWI is performed in prostate tissue over an extended range of *b*-values with multiple diffusion times compartment models incorporating both anisotropic and restricted components provide more information-rich descriptions of signals than single component models or multicomponent anisotropic models and models that do not account for restricted diffusion. These results highlight the limitations of the basic ADC and DTI models and demonstrate that appropriate DWI measurements can probe multiple tissue structure features.

Acknowledgements. This work was supported by Australian NHMRC grant 1026467 and European/UK grants EPSRC H046410, G00748 and CRUK/EPSRC C1519/ A16463

References

1. Guzzo TJ, Vira M, Hwang WT, D'Amico A, Tomaszewski J, Whittington R, Wein AJ, VanArsdalen K, Malkowicz SB. Impact of multiple biopsy cores on predicting final tumor volume in prostate cancer detected by a single microscopic focus of cancer on biopsy. Urology. 2005; 66(2): 361-365.
2. Nelson BA, Shappell SB, Chang SS, Wells N, Farnham SB, Smith JA, Jr., Cookson MS. Tumour volume is an independent predictor of prostate-specific antigen recurrence in patients undergoing radical prostatectomy for clinically localized prostate cancer. BJU International. 2006; 97(6): 1169-1172.
3. Hong MK, Namdarian B, Corcoran NM, Pedersen J, Murphy DG, Peters JS, Harewood L, Sapre N, Rzetelski-West K, Costello AJ. Prostate tumour volume is an independent predictor of early biochemical recurrence in a high risk radical prostatectomy subgroup. Pathology. 2011; 43(2): 138-142.
4. Kirkham AP, Haslam P, Keanie JY, McCafferty I, Padhani AR, Punwani S, Richenberg J, Rottenberg G, Sohaib A, Thompson P, Turnbull LW, Kurban L, Sahdev A, Clements R, Carey BM, Allen C. Prostate MRI: who, when, and how? Report from a UK consensus meeting. Clin. Radiol. 2013; 68(10): 1016-1023.
5. Dickinson L, Ahmed HU, Allen C, Barentsz JO, Carey B, Futterer JJ, Heijmink SW, Hoskin PJ, Kirkham A, Padhani AR. Magnetic resonance imaging for the detection, localisation, and characterisation of prostate cancer: recommendations from a European consensus meeting. Eur. Urol. 2011; 59(4): 477-494.
6. Padhani AR, Collins D, Hammoud DA, Rustin GJS, Taouli B, Choyke PL, Liu G, Koh DM, Chenevert TL, Thoeny HC, Takahara T, Dzik-Jurasz A, Ross BD, Van Cauteren M. Diffusion-weighted magnetic resonance imaging as a cancer biomarker: consensus and recommendations. Neoplasia. 2009; 11(2): 102-125.
7. Isebaert S, Van den Bergh L, Haustermans K, Joniau S, Lerut E, De Wever L, De Keyzer F, Budiharto T, Slagmolen P, Van Poppel H. Multiparametric MRI for prostate cancer localization in correlation to whole‐mount histopathology. J. Magn. Reson. Imaging. 2013; 37(6): 1392-1401.
8. Selnæs KM, Heerschap A, Jensen LR, Tessem M-B, Jarosch-Von Schweder G, Goa PE, Viset T, Angelsen A, Gribbestad IS. Peripheral zone prostate cancer localization by multiparametric magnetic resonance at 3 T: unbiased cancer identification by matching to histopathology. Invest. Radiol. 2012; 47(11): 624-633.
9. Turkbey B, Shah VP, Pang Y, Bernardo M, Xu S, Kruecker J, Locklin J, Baccala Jr AA, Rastinehad AR, Merino MJ. Is apparent diffusion coefficient associated with clinical risk scores for prostate cancers that are visible on 3-T MR images? Radiology. 2011; 258(2): 488-495.
10. LeBihan D. Molecular diffusion, tissue microdynamics and microstructure. NMR Biomed. 1995; 8(7): 375-386.
11. Epstein JI, Allsbrook Jr WC, Amin MB, Egevad LL, Committee IG. The 2005 International Society of Urological Pathology (ISUP) consensus conference on Gleason grading of prostatic carcinoma. Am. J. Surg. Pathol. 2005; 29(9): 1228-1242.
12. Bourne RM, Panagiotaki E, Bongers A, Sved P, Watson G, Alexander DC. Information theoretic ranking of four models of diffusion attenuation in fresh and fixed prostate tissue ex vivo. Magn. Reson. Med. 2014; 72(5): 1418-1426.

13. Hall MG, Bongers A, Sved P, Watson G, Bourne RM. Assessment of non‐Gaussian diffusion with singly and doubly stretched biexponential models of diffusion‐weighted MRI (DWI) signal attenuation in prostate tissue. NMR Biomed. 2015; 28(4): 486-495.
14. Shinmoto H, Oshio K, Tamura C, Soga S, Okamura T, Yamada K, Kaji T, Mulkern RV. Diffusion-weighted imaging of prostate cancer using a statistical model based on the gamma distribution. J. Magn. Reson. Imaging. 2015; 42(1): 56-62.
15. Shinmoto H, Oshio K, Tanimoto A, Higuchi N, Okuda S, Kuribayashi S, Mulkern RV. Biexponential apparent diffusion coefficients in prostate cancer. Magn. Reson. Imaging. 2009; 27(3): 355-359.
16. Rosenkrantz AB, Sigmund EE, Johnson G, Babb JS, Mussi TC, Melamed J, Taneja SS, Lee VS, Jensen JH. Prostate cancer: feasibility and preliminary experience of a diffusional kurtosis model for detection and assessment of aggressiveness of peripheral zone cancer. Radiology. 2012; 264(1): 126-135.
17. Panagiotaki E, Walker-Samuel S, Siow B, Johnson SP, Rajkumar V, Pedley RB, Lythgoe MF, Alexander DC. Noninvasive quantification of solid tumor microstructure using VERDICT MRI. Cancer Res. 2014; 74(7): 1902-1912.
18. Panagiotaki E, Chan R, Dikaios H, Ahmed HU, O'Callaghan J, Freeman A, Atkinson D, Punwani S, Hawkes D, Alexander D. Microstructural Characterization of Normal and Malignant Human Prostate Tissue With Vascular, Extracellular, and Restricted Diffusion for Cytometry in Tumours Magnetic Resonance Imaging. Invest. Radiol. 2015; 50(4):218-227.
19. Panagiotaki E, Andrada I, Johnston E, Chan R, Stevens N, Atkinson D, Punwani S, Hawkes D, Alexander D. Optimised VERDICT MRI Protocol for Prostate Cancer Characterisation. *Proceedings of the 23rd Annual Meeting ISMRM*, Toronto, Canada, 2015; 2872.
20. Bourne RM, Bongers A, Chatterjee A, Sved P, Watson G. Diffusion anisotropy in fresh and fixed prostate tissue ex vivo. Magn. Reson. Med. 2015: Early view. doi: 10.1002/mrm.25908.
21. Bourne RM, Kurniawan N, Cowin G, Sved P, Watson G. Microscopic diffusion anisotropy in formalin fixed prostate tissue: Preliminary findings. Magn. Reson. Med. 2012; 68(6): 1943-1948.
22. Bourne R, Bongers A, Charles N, Power C, Sved P, Watson G. Effect of formalin fixation on biexponential modeling of diffusion decay in prostate tissue. Magn. Reson. Med. 2013; 70(4): 1160-1166.
23. Dietrich O, Raya JG, Reeder SB, Reiser MF, Schoenberg SO. Measurement of signal‐to‐noise ratios in MR images: Influence of multichannel coils, parallel imaging, and reconstruction filters. J. Magn. Reson. Imaging. 2007; 26(2): 375-385.
24. Panagiotaki E, Schneider T, Siow B, Hall MG, Lythgoe MF, Alexander DC. Compartment models of the diffusion MR signal in brain white matter: a taxonomy and comparison. Neuroimage. 2012; 59(3): 2241-2254.
25. Basser PJ. Inferring microstructural features and the physiological state of tissues from diffusion-weighted images. NMR Biomed. 1995; 8(7): 333-344.
26. Cook P, Bai Y, Nedjati-Gilani S, Seunarine K, Hall M, Parker G, Alexander D. Camino: open-source diffusion-MRI reconstruction and processing. *Proceedings of the 14th Annual Meeting ISMRM*, Seattle, WA, USA, 2006; 2759.
27. Weingärtner H. Self diffusion in liquid water. A reassessment. Z. Phys. Chem. 1982; 132(2): 129-149.

28. Burnham KP, Anderson DR. *Model selection and multimodel inference: a practical information-theoretic approac*h. Springer Science & Business Media; 2002.
29. Holz M, Heil SR, Sacco A. Temperature-dependent self-diffusion coefficients of water and six selected molecular liquids for calibration in accurate 1H NMR PFG measurements. Phys. Chem. Chem. Phys. 2000; 2(20): 4740-4742.
30. Le Bihan D, Breton E, Lallemand D, Aubin ML, Vignaud J, Lavaljeantet M. Separation of diffusion and perfusion in intravoxel incoherent motion MR imaging. Radiology. 1988; 168(2): 497-505.
31. Jambor I, Merisaari H, Taimen P, Boström P, Minn H, Pesola M, Aronen HJ. Evaluation of different mathematical models for diffusion-weighted imaging of normal prostate and prostate cancer using high b-values: A repeatability study. Magn. Reson. Med. 2015; 73(5): 1988-1998.
32. Xu JQ, Humphrey PA, Kibel AS, Snyder AZ, Narra VR, Ackerman JJH, Song SK. Magnetic Resonance Diffusion Characteristics of Histologically Defined Prostate Cancer in Humans. Magn. Reson. Med. 2009; 61(4): 842-850.
33. Richardson S, Siow B, Panagiotaki E, Schneider T, Lythgoe MF, Alexander DC. Viable and fixed white matter: Diffusion magnetic resonance comparisons and contrasts at physiological temperature. Magn. Reson. Med. 2014; 72(4): 1151-1161.
34. Storas T, Bongers A, Power C, Bourne R. Effect of Formalin Fixation on Biexponential Modeling of T1 and T2 Decay in Prostate Tissue. *Proceedings of the 21st Annual Meeting ISMRM*, Salt Lake City, Utah, USA, 2013; 1792.
35. Storas TH, Gjesdal KI, Gadmar OB, Geitung JT, Klow NE. Prostate Magnetic Resonance Imaging: Multiexponential T2 Decay in Prostate Tissue. J. Magn. Reson. Imaging. 2008; 28(5): 1166-1172.

Tables

Table 1. DWI acquisition parameters

Prostate	1	2		3			4	
FOV (mm^2)	64×50	64×50		50×50			45×45	
Matrix size	32×25	32×25		50×50			45×45	
Voxel size (mm^3)	2×2×4	2×2×4		1×0.78×2			1.4×1.4×2	
SNR	225	232		291			240	
TR (ms)	2000	2000		2000			2000	
δ (ms)	5	5	10	5	5	10	5	10
Δ (ms)	10, 20, 40, 60, 80	10, 20, 40, 60, 80	40, 60, 80	10	20, 40	20, 40	20, 40, 80	20, 40, 80
TE (ms) (=Δ + 8 ms)	18, 28, 48, 68, 88	18, 28, 48, 68, 88	93, 93, 93	18	28, 48	33, 53	28, 48, 88	28, 48, 88
b-value (s/mm^2) 6-directions	1500	1500		1500			1599	
b-value [a] (s/mm^2) 3-directions	50, 147, 275, 430, 607, 806, 1024, 1259, 1512, 1780, 2064, 2362, 2674, 3000	50, 147, 275, 430, 607, 806, 1024, 1259, 1512, 1780, 2064, 2362, 2674, 3000	50, 147, 275, 430, 607, 806, 1024, 1259, 1512, 1780, 2064, 2362, 2674, 3000	50, 178, 373, 632, 951, 1328, 1761, 2249, 2790, 3384, 4029, 4724, 5470, 5960	50, 178, 373, 632, 951, 1328, 1761, 2249, 2790, 3384, 4029, 4724, 5470, 6265, 7108, 8000	216, 511, 940, 1507, 2217, 3073, 4077, 5231, 6538	105, 279, 589, 1044, 1646, 2403, 3318, 4394, 5631, 7036, 8610, 10354	105, 279, 589, 1044, 1646, 2403, 3318, 4394, 5631, 7036, 8610, 10354

a) Nominal *b*-value. Effective *b*-values were used for model fitting.

Table 2. Model components

Name	Description	Parameters [a]
Ball (ADC)	Isotropic Gaussian diffusion	S_0 D
Zeppelin	Anisotropic cylindrically symmetric Gaussian diffusion	S_0 $D_{\|}$ $D_{\perp}$ θ ϕ
Tensor	Anisotropic Gaussian diffusion	S_0 $D_{\|}$ $D_{\perp 1}$ $D_{\perp 2}$ θ ϕ α
Sphere	Restricted diffusion inside an impermeable spherical confinement of non-zero radius *R*	S_0 D R

a) S_0, the signal at b = 0, is omitted if signal is normalized. D is a diffusivity and θ, ϕ, α are tensor angles. Detailed parameter descriptions are provided in (24)

Table 3. Fitted models

Name	Components from Table 2	Fitted parameters [a]	No. parameters
Ball (ADC)	Ball	D	1
Bi-ball	Ball + Ball	$f_1 \quad D_1 \quad D_2$	3
Ball-sphere	Ball + Sphere	$f_1 \quad D_1 \quad R \quad D_2$	4
DTI	Tensor	$D_{\parallel} \quad D_{\perp 1} \quad D_{\perp 2} \quad \theta \quad \phi \quad \alpha$	6
Ball-zeppelin	Ball + Zeppelin	$f_1 \quad D_{\parallel} \quad D_{\perp} \quad \theta \quad \phi \quad D$	6
Zeppelin-sphere	Zeppelin + Sphere	$f_1 \quad D \quad R \quad D_{\parallel} \quad D_{\perp} \quad \theta \quad \phi$	7
Ball-tensor	Ball + Tensor	$f_1 \quad D_{\parallel} \quad D_{\perp 1} \quad D_{\perp 2} \quad \theta \quad \phi \quad \alpha \quad D$	8
Bi-ball-zeppelin	Ball + Ball + Zeppelin	$f_1 \quad f_2 \quad D_1 \quad D_2 \quad D_{\parallel} \quad D_{\perp} \quad \theta \quad \phi$	8
Bi-zeppelin	Zeppelin + Zeppelin	$f_1 \quad D_{\parallel 1} \quad D_{\perp 1} \quad \theta_1 \quad \phi_1 \quad D_{\parallel 2} \quad D_{\perp 2} \quad \theta_2 \quad \phi_2$	9
Tensor-sphere	Tensor + Sphere	$f_1 \quad D_{\perp 1} \quad D_{\perp 2} \quad \theta \quad \phi \quad \alpha \quad D \quad R$	9

a) Signal normalized before fitting ($S_0 = 1$). Sum of signal fractions $f_1 + f_2 + f_n = 1$. Parameter descriptions are detailed in (24).

Figure Captions

Figure 1. Variation of model rankings in four prostates.

A) Anatomical distribution of the highest ranked model in a mid-organ slice from each prostate. (See Fig. 2 for pathology maps of these slices). Voxel color indicates model according to the Model key. The Zeppelin-sphere (yellow) or Tensor-sphere (orange) models ranked highest in most voxels in all prostates.

B) Variation of model rank positions. The grey scale indicates the number of times each model ranked at each position (eg. the Ball model ranked 10th in nearly all voxels). The model order (vertically) is based on trends assessed subjectively. See Fig. 3 for statistical summary of AIC ranks.

Data from 558 voxels from slices 5&6 in Prostate 1, 504 voxels from slices 5&6 in Prostate 2, 1278 voxels from slices 7-9 in Prostate 3, and 2041 voxels from slices 3-6 in Prostate 4.

Model Key: The three models containing a restricted component are shown with a heavy black border. Models with an anisotropic component are shown as ellipses. Vertical lines indicate number of components. Models including a restricted component are marked with an asterisk.

Figure 2. Variation in rankings of individual models in four prostates.
Slice positions as for Figs 1 and 5. Voxel color indicates model rank and models are grouped according to predominant rank.

Figure 3. Box and whiskers plots of log(AIC).

Models including a restricted component are marked with a black asterisk. For each blue box, the central red mark is the median and the top and bottom edges of the box are the 25th and 75th percentiles. The whiskers extend to the most extreme data points that are not considered outliers. Outliers are plotted individually in red.
Distributions were normal after the log transformation. Data from 558 voxels from slices 5&6 in Prostate 1, 504 voxels from slices 5&6 in Prostate 2, 1278 voxels from slices 7-9 in Prostate 3, and 2041 voxels from slices 3-6 in Prostate 4. Results for Mann-Whitney U-test are presented in Supplementary Material available online.

Figure 4. Representative model fit data.
Measurement data (symbols) and model fit (lines). Normalized signal *S* is plotted for all values of Δ and δ as a function of gradient strength |G| for x, y, z directions. Indicated model rank is specific to this data set. Measurement data (SNR ~600) is the average from four adjacent $1{\times}0.78{\times}2$ mm^3 voxels in the transition zone of Prostate 3 with similar primary eigenvector orientation as assessed by the DTI model.

Figure 5. Zeppelin-sphere model parameter maps.

Slice positions as for Figs. 1&2. Parameter maps for the Tensor-sphere model for the same slices are provided in Supporting Figure S1. For reference the Ball *D* (ADC) parameter maps are included.

Figure 6. Two-way parameter histograms for Zeppelin-sphere model.

Pixel brightness proportional to voxel count. Note that when a component's signal fraction is low the parameter estimates for that component may be unreliable. The majority of voxels in each of the four prostates have biophysically plausible parameter values.

Figure S1. Tensor-sphere model parameter maps.

Slice positions as for Figs. 1&2.

Figure S2. One-way parameter histograms for Zeppelin-sphere model.

Table S1. *P*-values from Mann-Whitney U-test.

Insignificant differences ($P > 0.05$) between models are shown in bold type.
1 – Ball, 2 – Bi-ball, 3 – Ball-zeppelin, 4 – Bi-ball-zeppelin, 5 – Zeppelin-sphere,
6 – Bi-zeppelin, 7 – Tensor-sphere, 8 – Ball-sphere, 9 – Ball-tensor, 10 – DTI

NBM-15-0318.R1 Response to reviewers

Reviewer: 1

> The manuscript is now concise and clear enough with "aims...quite modest" so is publishable though a) I do not see how normalizing to b = 0 minimizes T2 effects, I don't think it does at all and b) the authors never discussed simple diffusion dependence vs Delta (diffusion time) from their data. A careful look at the 9 decay curves (3 directions, 3 Deltas) in Figure 4 actually shows that for the largest Delta (also largest TE) the overall decays are quicker (higher diffusion) than the more slowly decaying signals at shortest Delta (10 ms) and shortest TE. Maybe at the higher TE, more free water is being encountered and so decays with b are quicker. This is all outside the scope of which models "ranks" best and it is nice to see that models with both anisotropic and retsricted diffusion effects fare best BUT it would have been nice to have some of the above observations commented upon - if only briefly as I do think T2 is playing a role here.

We agree with the reviewer that there may be T2 effects however there is no direct evidence of these in our data. We follow the convention of the cited references (using the same modeling techniques) of minimizing T2 effects through normalization to the b=0 signal at each TE. This means we are mainly modeling signal decay due to increased diffusion weighting and any total signal variations due to TE differences are reduced.

Accounting for possible T2 effects would make the models much more complex - especially when it cannot be assumed that multiple T2 spin pools may not be identical to the two diffusion pools identified. There is, at present, no biophysical argument for simply adding a T2 decay term to the signal for each of the distinct diffusion components. We note in our text the neglect of possible T2 effects as a limitation of the study and that it is a topic worthy of further investigation.

We are unsure what the reviewer intended with the statement: “Maybe at the higher TE, more free water is being encountered and so decays with b are quicker”.

Given the presence of a significant unrestricted spin pool it is to be expected that the total signal will decay faster at the longer diffusion times.

We do not specifically discuss diffusion time dependence of our signals as this is inherent in the definition of the restricted diffusion compartment. We have added a sentence to this effect under “Model Fitting” in Methods.

> Reviewer: 2

> The authors have taken most comments into account and this results in an improved paper. It is good to see that the authors have included more statistics and removed some of the results and discussion that were based on a small number of prostate cancers. There are some issues that remain.
> - A good explanation for the choice of b-factors, echo-times and delta’s is missing in the method section. The authors commented on this in their response to the reviewers, but this information should also be available to the readers.

We have added explanatory text to the first paragraph of "MR Imaging" in the Methods section. Also added a sentence on significance voxel size independence of the model ranking has been added to the Discussion.

> - It's admirable that the authors added figure 6, which is a two-way histogram that provides info about the parameter values and fractions. However, in the current shape it is quite difficult to interpret the different intensities. Would it be possible to limit this figure to a one way histogram that only shows the distribution of D and R, without the information about the fraction?

Histograms of D and R for the zeppelin-sphere model have been added as supplementary Figure S2.

> - Last sentence of the results – make a reference to figure 6 or provide an average sphere radius value.

Done.

> Reviewer: 3

> The authors have addressed the points raised by the reviewers. Where possible they have altered the manuscript to comply with the reviewer requests. They have also limited the interpretations made from the results such that they are now more in line with the nature of the paper.
> The major limitation of the study remains that the sample size is small. As such the inferences of the work remain limited. Nonetheless, the paper does highlight some potential avenues for developing diffusion weighted imaging for the evaluation of prostate cancer.